ANNALS OF GEOPHYSICS, 66, 6, SE638, 2023; doi:10.4401/ag-8985
OPEN ACCESS

ELSEM-Net, a network of ground-based telemetric stations for the monitoring of fracture-induced electromagnetic emissions in Greece: Instrumentation, management and analysis of recent observations associated with strong earthquakes

Filopimin Malkotsis[1,2], Nikolaos Papadopoulos[1], Dimitrios Z. Politis[1], Dionysios Dimakos[1,2], Michael Exarhos[1], Efstratios Liadopoulos[3], Yiannis Contoyiannis[1], Angelos Charitopoulos[1], Kyriakos Kontakos[3], Grigorios Koulouras[1], Nikolaos Melis[3], Konstantinos Eftaxias[4], Stelios M. Potirakis[*,1,5]

(1) Department of Electrical and Electronics Engineering, Ancient Olive Grove Campus, University of West Attica, Aigaleo-Athens, GR-12241, Greece
(2) Hellenic Telecommunications and Post Commission (EETT), 60 Kifissias Avenue, Marousi-Athens, GR-15125, Greece
(3) Institute of Geodynamics, National Observatory of Athens, Lofos Nimfon, Thissio-Athens, GR-11810, Greece
(4) Department of Physics, University of Athens, Panepistimiopolis, GR-15784, Zografos-Athens, GR-15784, Greece
(5) Institute for Astronomy, Astrophysics, Space Applications and Remote Sensing, National Observatory of Athens, Metaxa and Vasileos Pavlou, Penteli-Athens, GR-15236, Greece

Article history: received May 31, 2023; accepted July 25, 2023

Abstract

The hELlenic Seismo-ElectroMagnetics Network (ELSEM-Net, http://elsem-net.uniwa.gr) is a network of telemetric stations spanning all over Greece for the monitoring of fracture-induced electromagnetic emissions (FEME), often also referred to as electromagnetic radiation (FEMR). At the laboratory scale, it has been proved that FEME/FEMR are produced by opening cracks in a wide frequency spectrum ranging from the MHz to the kHz bands as the general (macroscopic) fracture is approaching, rendering them precursors of general fracture that permit the monitoring of the gradual damage of stressed materials. FEME/FEMR is also observed at the geophysical scale, preceding strong earthquakes (EQs) with epicenters on land or near the coast-line. Based on the idea that MHz-kHz FEME/FEMR should also permit the monitoring of the gradual damage of stressed materials in the Earth's crust, as it happens in the laboratory experiments, ELSEM-Net was gradually developed from 1992 to 1998 and currently comprises 11 stations installed in various locations in Greece. Here we present the instrumentation that has been specifically designed for ELSEM-Net, both hardware and firmware/software, as well as a web-based system for the management of the field stations, the recorded data, and the automated preliminary analysis results. Finally, we present the analysis of selected observations associated with recent strong earthquakes that hit Greece, using a most recently introduced time series analysis method. Our presentation aims to communicate in detail the experimental infrastructure behind our almost 30 years of research in geophysical scale FEME/FEMR so that other interested research groups around the world can take advantage of it and have the opportunity to install similar

stations/networks in other locations of the world for the study of pre-EQ processes associated with natural or man-induced seismicity.

Keywords: Earthquakes; Fracture-induced electromagnetic emissions; Fracture-induced electromagnetic radiation; Seismo-electromagnetics; Ground-based observatories' network

1. Introduction

Earthquakes (EQs) are perceived as sudden, violent tremors of the Earth's surface, which, depending on the hypocenter location and the magnitude, can have multiple devastating consequences to the society and economy, such as material damages (to infrastructures, company losses, personal properties, etc.) and injuries or even loss of lives, [e.g., Yuan, 2008; Kazama and Noda, 2012; Kalligeris et al. 2022; Dolu and İkizler, 2022; Naddaf, 2023; Nature Editorial, 2023]. Due to their potentially catastrophic consequences, EQs attract the interest of the society and scientists, as it happens for all natural disasters, e.g., [Keller and DeVecchio 2019].

The preparation of an EQ involves various interrelated complex processes, not all of which are yet fully understood, not all of them offering direct observables, while the regularity of direct or indirect EQ-related observables is not yet clear, [e.g., Li et al., 2021; Elliott et al., 2020; Ke et al., 2022; Li and Cai, 2022; Brener and Bouchbinder, 2021]. The understanding of EQ preparation through the study of possibly EQ-related phenomena that offer observables, [e.g., Pulinets et al., 2022; Picozza et al., 2021; Pritchard et al., 2020; Chelidze et al., 2018; Pulinets and Ouzounov, 2018; Hayakawa et al., 2022; Martinelli, 2020; Zhao et al., 2021], is a challenging task for the scientists working in this interdisciplinary research field. Although several hypotheses have been formulated about the involved physical/chemical mechanisms, and some of them are supported to a greater or lesser degree by observables and their analysis, it could be said that the topic is still considered controversial [Geller, 1997; Joffe et al., 2017; Vance, 2018]. However, a way to achieve, at some point, credible and precise EQ forecasting might be to gain the maximum understanding of EQ preparation and EQ-related phenomena. In our opinion, this requires the study of all available observables and the combination of the information acquired from all possible sources through the wide osmosis between scientists of different disciplines investigating these phenomena from different points of view. In this direction, it is of key importance the accumulation of adequate amounts of data over time that will eventually allow for statistical evaluation of the possible correlation between the occurrence of certain types of phenomena, as manifested by their observables and their analysis, and the occurrence of an EQ. This view led to the deployment and long (> 20 years) operation of the hELlenic Seismo-ElectroMagnetics Network (ELSEM-Net, http://elsem-net.uniwa.gr (last accessed on 14 May 2023)), a network of telemetric stations spanning all over Greece for the monitoring of fracture-induced electromagnetic emissions.

The field known as ''seismo-electromagnetics'', covers various electromagnetic phenomena possibly related to EQs, [e.g., Zhao et al., 2022; Huang et al., 2020; Venegas-Aravena et al., 2019; Sharma et al., 2020; Sorokin et al., 2020; Zhang et al., 2023a; 2023b; Schekotov et al., 2021; Hayakawa et al., 2002; 2010; Hayakawa, 2019; Huan et al., 2009; Uyeda et al., 2009a, 2009b; Pulinets and Boyarchuk, 2005; Varotsos, 2005; Molchanov and Hayakawa, 2008; Hattori, 2013; Eftaxias and Potirakis, 2013; Uyeda, 2013; Hayakawa, 2015]. Fracture-induced electromagnetic emissions (FEME), often also referred to as electromagnetic radiation (FEMR), hereafter quoted as FEME/FEMR, when studied at the geophysical scale, are also classified in this research field. FEME/FEMR presents some very interesting features:

a) They are found in different scales of fracture, namely, at the small/ laboratory scale (fracture experiments), at the large/geophysical scale (natural EQs), as well as in intermediate scale failures (man-induced EQs related to mining, fracking, land sliding, etc.), [e.g., Sharma et al., 2020; Das et al., 2020; Lacidogna et al., 2010; Hadjicontis et al., 2011; Carpinteri et al., 2011; Rabinovitch et al., 2017; Li et al., 2022; Daniliev et al., 2022; Frid et al., 2006; 2020a, 2020b, 2021; Frid and Vozoff, 2005; Song et al., 2018; Martinelli et al., 2020; Lin et al., 2021; Yoshida and Ogawa, 2004; Lei and Satoh, 2007; Guo et al., 2021; Gokhberg et al., 1982; Enomoto and Hashimoto, 1990; Fraser-Smith et al., 1990; Carpinteri and Borla, 2017; Yoshiro, 1991; Gershenzon et al., 1989; Greiling and Obermeyer, 2010; Nomikos et al., 1997; Nomikos and Vallianatos, 1998; Vallianatos and Nomikos, 1998; Eftaxias

et al., 2001; 2002; 2004; 2018; Contoyiannis et al., 2005; Contoyiannis and Potirakis, 2018; Potirakis et al., 2016; 2019a; 2021; 2022].

b) An important feature, observed both at laboratory and geophysical scale FEME/FEMR, is that the MHz radiation systematically precedes the kHz one, [e.g., Ohnaka and Mogi, 1982; Qian et al., 1994; Kumar and Misra, 2007; Eftaxias et al., 2002 (and references therein), 2004; Kapiris et al., 2004a; 2004b; Contoyiannis et al., 2005; Baddari and Frolov, 2011; Lacidogna et al., 2010; Eftaxias et al., 2018].
c) Although the geophysical scale FEME/FEMR signals have been much more intensively studied than the FEME/FEMR at other fracture scales, there are already indications that they may present similar features in terms of complex systems time series analysis (where, of course, such analysis methods can be applied to FEME/FEMR at different fracture scales, e.g., due to limitations in the duration of the phenomenon, available sampling rate, and different kind of used instrumentation), [e.g., Mastrogiannis et al., 2020; Potirakis and Mastrogiannis, 2017; Potirakis et al., 2021].
d) In both laboratory and geophysical scales FEME/FEMR silence appears before the global rupture, [e.g., Eftaxias et al., 2013; 2018; Eftaxias and Potirakis, 2013; Lacidogna et al., 2010, and references therein].
e) In both laboratory and geophysical scales FEME/FEMR silence appears after the global rupture, [e.g., Eftaxias et al., 2018; Eftaxias et al., 2013; Eftaxias and Potirakis, 2013, and references therein].

Although the FEME/FEMR at the intermediate scale is not so intensively studied, one cannot ignore the above-mentioned analogies between fractures at different scales. So, one cannot exclude the possibility that the mechanism of EQs is some sort of laboratory fracture process, as it has already been early suggested [Eftaxias and Potirakis, 2013, and references therein]. At this point it should be mentioned that FEME/FEMR, as well as acoustic emissions (AE) are both detected at the laboratory scale [e.g., Ohnaka and Mogi, 1982; Yoshida and Ogawa, 2004; Lacidogna et al., 2010; Hadjicontis et al., 2011; Carpinteri et al., 2011; Carpinteri and Borla, 2017], while AE can be considered analogous to foreshock seismicity [Eftaxias et al., 2018; Eftaxias et al., 2013; Eftaxias and Potirakis, 2013]. On the other hand, it is highlighted that it is often difficult to study the kinetics of brittle rocks' fracture in the laboratory, due to the rapid unstable fracture growth in the last and more interesting stages. At the laboratory scale, the fault growth process normally occurs violently in a fraction of a second. Therefore, crucial information probably is lost. A major difference between laboratory and natural processes is the order-of-magnitude differences in scale (in space and time), allowing the possibility of experimental observation at the geophysical scale, for a range of physical processes, which are not observable at the laboratory scale. Thus, the idea that field observations by means of FEME/FEMR will probably reveal features of the last crucial stages of EQ generation, which are not clearly observable at the laboratory scale, in principle, cannot be excluded.

Under the above-mentioned assumptions, the acquisition of electromagnetic field variations in the MHz and kHz bands by ELSEM-Net and the multidisciplinary analysis of the acquired time series by multiple methods, aiming at the identification of specific statistical and dynamical characteristics which render particular time series excerpts valid MHz or kHz FEME/FEMR, has been the focus of our research. Published results over the past $>$ 20 years indicate that the MHz-kHz FEME/FEMR precursors recorded by ELSEM-Net contain rich information about the last stages of an ensuing seismic event, vindicating the assumptions which led us to develop the specific experimental network for the study of fracture at the geophysical scale. Summarizing our research results on this field, a four-stage model for EQ generation (FSMEG) in terms of FEME/FEMR has recently been proposed, [e.g., Contoyiannis et al., 2005; 2015; Donner et al., 2015; Eftaxias et al., 2013; 2018; Potirakis et al., 2019a; 2022]:

First stage:
The initially observed MHz FEME/FEMR is due to the fracture of the highly heterogeneous system that surrounds the formation of strong brittle and high-strength entities (asperities) distributed along the rough surfaces of the main fault sustaining the system. The MHz FEME/FEMR can be described by means of a second-order phase transition in equilibrium. The appearance of the symmetry-breaking phenomenon signifies the departure from the critical state.

Second stage:
The appearance of tri-critical behavior in the final stage of MHz FEME/FEMR, or in the initial stage of kHz FEME/FEMR, or in both, signalizes a next, distinct, state of the EQ preparation process towards a first-order phase transition.

Third stage:
The finally abruptly emerging strong sequence of kHz FEME/FEMR avalanches originates in the stage of stick–slip-like plastic flow, namely, the fracture of asperities themselves. The burst-like kHz FEME/FEMR does not present any footprint of a second-order transition in equilibrium but, beyond their other features, present first-order phase transition characteristics.

Fourth stage:
Finally, the systematically observed EM silence in all frequency bands before the time of the EQ occurrence is sourced in the process of preparation of the dynamical slip which results in the fast, even super-shear, mode that surpasses the shear wave speed and corresponds to the observed EQ tremor.

The proposed model has been tested, in a series of relevant publications, [e.g., Eftaxias et al., 2001; 2004; 2008; 2018; Potirakis et al., 2011; 2012a; 2012b; 2012c; 2013; 2015; 2016, 2019a; 2019b; 2021; 2022; Kapiris et al., 2004a; Karamanos et al., 2006; Papadimitriou et al., 2008; Contoyiannis et al., 2005; Eftaxias and Potirakis, 2013; Minadakis et al., 2012a; 2012b], by means of: (i) recent laboratory studies; (ii) statistical physics, especially phase transitions, critical phenomena, Lévy and Gauss statistics, and non-extensive statistical physics, (iii) self-similarity, which is a basic feature of fracture and faulting offering universal fingerprints that should be included in a candidate precursor; (iv) theoretical model of EQ dynamics and numerical studies; (v) fractal electrodynamics; (vi) tools from information theory; (vii) memory effects; (viii) friction phenomena at seismic slip velocities, which is now a frontier in tectonophysics; (ix) their agreement with other precursors coming from other disciplines.

In this paper, the ELSEM-Net is for the first time thoroughly presented, so that more research groups around the world could take advantage of it and have the opportunity to install similar stations/networks at other locations of the world for the study of pre-EQ processes associated with natural or man-induced seismicity in terms of MHz-kHz FEME/FEMR. Specifically, in the rest of the paper: Section 2 briefly presents the development history and current status of ELSEM-Net. Section 3 presents in detail the hardware (HW) used in the field stations, including specifically designed receivers (see Section 3.1), antennas (see Section 3.2), and a new "Single-Board Computer – Expansion Board" architecture datalogger (see Section 3.3). The ELSEM-Net software (SW) is presented in Section 4, i.e., the website that is specifically designed to act as a collaboration platform (see Section 4.1) and the data management scheme (see Section 4.2). Section 5, presents an example of the analysis performed on ELSEM-Net recordings using a most recently introduced analysis method, while the conclusions are summarized in Section 6.

2. The network ELSEM-Net: Development history and current status

During 1992-1995, the first pilot network comprising 4 remote telemetric stations for the recording of electromagnetic variations in the MHz and kHz bands was put in operation along the Island of Crete, south Greece, while since 1994, an exemplary telemetric station has been operating on Zakynthos (Zante) Island (Greece) (see supplementary downloadable material of [Potirakis et al., 2015]) under the guidance of Prof. C. Nomicos and Prof. K. Eftaxias, mainly aiming at the detection of MHz-kHz EME/FEMR (see Section 1). From 1995 to 1998 the telemetric network was gradually expanded all over Greece, mostly installed at the field facilities (seismic stations) of the Hellenic Seismic Network (HL), which is operated by the Institute of Geodynamics of the National Observatory of Athens (NOA-IG) (https://bbnet.gein.noa.gr/HL/) (last accessed on 14 May 2023). The number of ELSEM-Net stations has been changing (increasing or decreasing) over the years since new locations are evaluated and others were assessed as inefficient after a few years of operation. The latest years 11 ELSEM-Net remote telemetric stations are in full unattended operation (see Table 1).

The specific frequencies at which the narrowband sensing of the kHz magnetic field and the MHz electric field is performed resulted after exhaustive field investigations to find "quiet" (of low man-made electromagnetic noise) frequency slots. Indeed, according to the official National Frequency Allocation Table (NFAT) [Department of National Defense and Department of Transport and Communications, 2006], the selected kHz frequencies (3 kHz and 10 kHz) should be "quiet". Specifically, 3 kHz have not been allocated, whereas 10 kHz have been awarded either to low-power, short-range applications or to rarely exercised applications (industrial, scientific, and medical applications, as well as radio navigation), ensuring minimum electromagnetic interference (EMI) sourced from human activities. Unfortunately, the MHz band is stuffed by FM radio broadcasting (87.5-108 MHz). However, the

No.	Station Code	Station Location	Latitude (° N)	Longitude (° E)	Altitude (m)
1	T	Komotini	41.1450	25.5355	116
2	K	Kozani	40.3033	21.7820	791
3	J	Ioannina	39.6561	20.8487	526
4	M	Agia Paraskevi, Lesvos Island	39.2456	26.2649	130
5	H	Atalandi, Lokrida	38.6495	22.9988	185
6	F	Valsamata, Cephalonia Island	38.1768	20.5886	402
7	Z	Fterini-Aghios Leon, Zakynthos Island	37.7658	20.7430	461
8	O	Ithomi, Mesinia	37.1787	21.9252	423
9	A	Archangelos, Rhodes Island	36.2135	28.1212	148
10	V	Vamos, Crete Island	35.4070	24.1997	225
11	E	Neapoli, Crete Island	35.2613	25.6103	288

Table 1. Locations of the remote FEME/FEMR stations of ELSEM-Net spanning all over Greece (see also Figs. 19 and 23 for the locations' depiction on the map).

locations of the remote telemetric stations have been selected to be in the range of kilometers away even from residential areas, usually in isolated mountainous sites. Moreover, as it has been verified by field measurements, there is very low human-made electromagnetic noise at the selected MHz frequencies of 41 MHz and 46 MHz (according to [Department of National Defense and Department of Transport and Communications, 2006], these frequencies are reserved for defense systems). At this point it should be mentioned that one should periodically check for man-made electromagnetic noise at the monitored frequencies, since human activities continuously expand, while new "noisy" devices burden the electromagnetic environment, such as LED road lights, etc.

The equipment used in these stations was gradually developed up to the form that we present here. Although hints about the early receiver designs can be found in some early publications of Prof. Nomicos' team [Vallianatos and Nomikos, 1998; Nomikos et al., 1995, 1997; Nomikos and Vallianatos, 1998; Koulouras et al., 2005a; Stavrakas et al., 2007], this is the first time that the ELSEM-Net instrumentation for the reception of the electromagnetic field variations in the MHz and kHz bands, with the aim of detection of geophysical scale FEME/FEMR, is presented in a complete and detailed way (see Sections 3 and 4).

Examples of MHz and kHz FEME/FEMR that have been acquired by ELSEM-Net are shown in Figure 1. An amazing coincidence between the behavior of the FEME/FEMR measured during laboratory fracture experiments and the pre-seismic ones observed by ELSEM-Net, regarding the sequential appearance of the MHz FEME/FEMR, followed by the kHz FEME/FEMR, and the finally observed electromagnetic silence after the kHz FEME/FEMR and before the fracture/EQ occurrence, as well as after the EQ occurrence, has been repeatedly verified (see Section 1). Note that, as it has repeatedly been clarified, all the pre-seismic FEME/FEMR that have been detected by ELSEM-Net are associated with shallow EQs that occurred on-land or near the coastline, [e.g., Eftaxias and Potirakis, 2013; Eftaxias et al., 2018], and references therein.

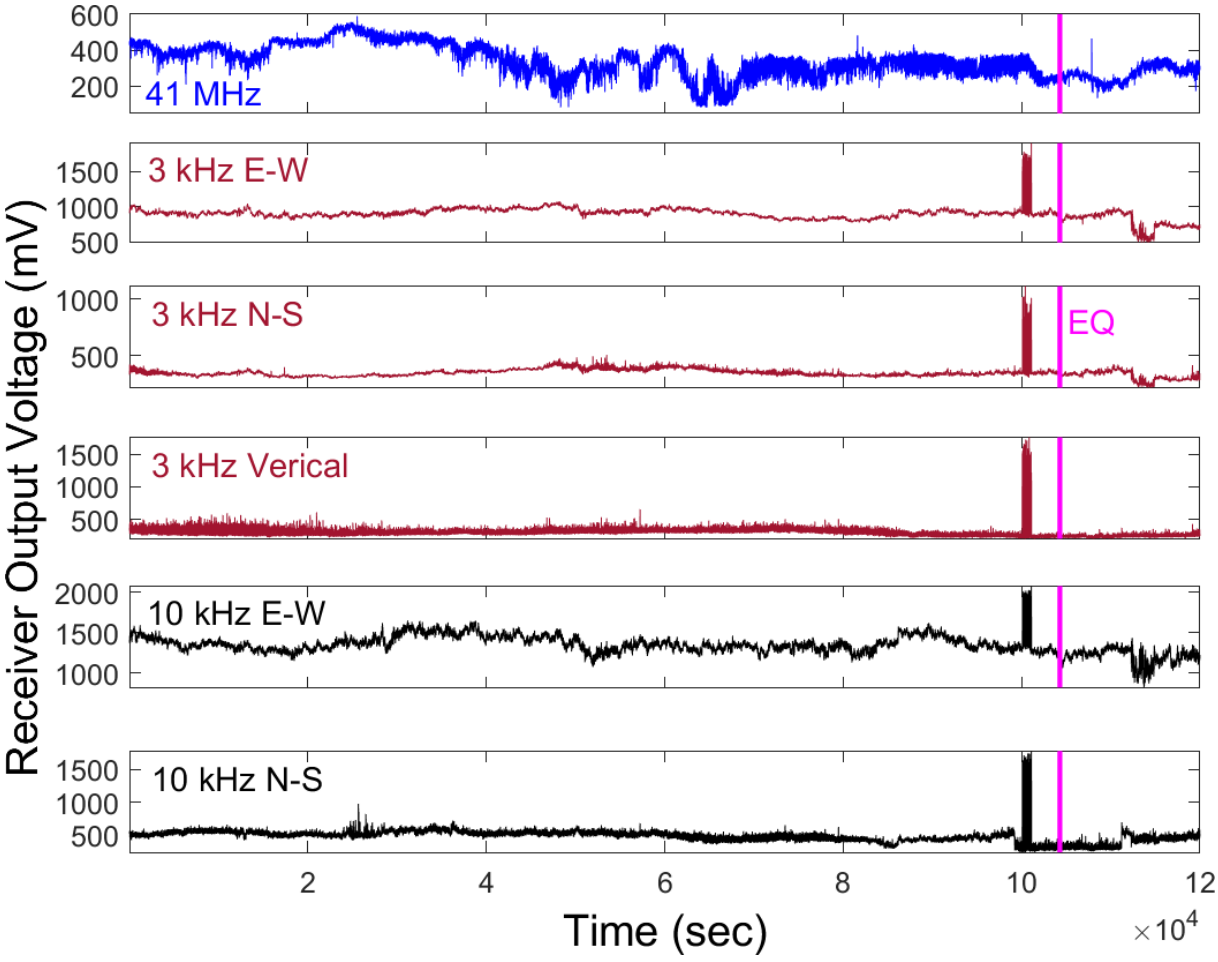

Figure 1. Characteristic signals acquired by ELSEM-Net. The specific signals were acquired prior to the Kozani-Grevena EQ, which occurred on 13/05/1995 in Northern Greece with a magnitude of 6.5. The specific signals have been analyzed in several publications, [e.g., Eftaxias et al., 2002; Potirakis et al., 2013; Eftaxias and Potirakis 2013; Contoyiannis et al., 2005; 2013], and references therein. It is worth noting that unlike the burst, avalanche-like, kHz FEME/FEMR, the MHz FEME/FEMR cannot be visually identified, but need elaborated non-linear time series analysis to be identified.

3. ELSEM-Net Hardware

The block diagram of a standard telemetric field station of ELSEM-Net is presented in Fig. 2. It comprises of four small loop antennas, with corresponding receivers for the monitoring of two components, East-West (E-W) and North-South (N-S), of the variations of the magnetic field at 3 kHz and 10 kHz, respectively, as well as two $\lambda/2$ electric dipole antennas for the monitoring of the electric field variations at 41 MHz and 46 MHz, respectively. All receiver outputs are simultaneously sampled by a multichannel datalogger once per second, i.e., with a sampling frequency of 1 Hz. At this point, it should be mentioned that an extended version of the above-described field station setup, with two more kHz channels, one more MHz channel, as well as other electromagnetic sensors, was installed in the exemplary telemetric station of Zakynthos (Zante) Island (Greece) (see supplementary downloadable material of [Potirakis et al., 2015]). The acquired time series, in the form of appropriately structured ASCII text or CSV files, are transferred through the internet to a network-attached storage (NAS) device, physically located in the University of West Attica (UniWA), Athens, Greece, for storage and management. Detailed information on all components of the specific setup is provided in the following Sections.

It has to be mentioned that very recently, new features of the ELSEM-Net have been briefly presented in Politis et al., [2023], but herein both the new features, as well as those that are successfully operating for many years, and are presently still in use, are presented in detail in Sections 3 and 4.

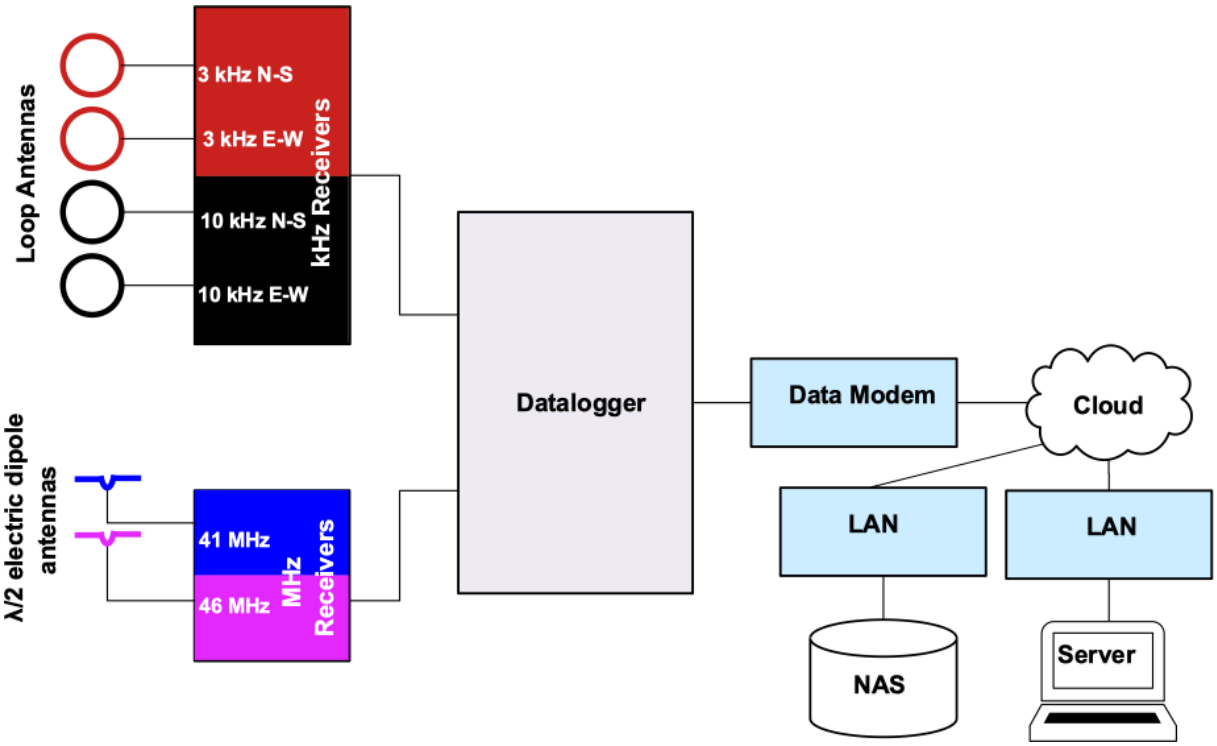

Figure 2. Block diagram of a standard ELSEM-Net telemetric station.

3.1 Receivers Design and Implementation

The ELSEM-Net receiver-related HW is based on two parametric-HW, custom designed, receivers, one for the kHz frequencies and one for the MHz frequencies, which use low-cost commercial components. By choosing specific passive components each receiver is working at one of the two, kHz or MHz, desired frequencies using the appropriate antennas (cf. Sec. 3 and Sec. 3.2). Figure 3 shows the main units and subunits of the receiver-related HW of a standard ELSEM-Net station. Note that the implemented printed circuit boards (PCBs) are portrayed by blocks of different colors in Fig. 3. A full receiver system comprises two units, the kHz receiver unit, and the MHz receiver unit.

In each one of these units a regulated power supply subsystem, as well as the receiver subsystems are implemented. The receiver subsystems are realized on daughterboard PCBs, each of them carrying the receivers for a specific kHz or MHz frequency. Specifically, the kHz receiver unit comprises two 3-channel kHz PCBs on which the kHz receivers are implemented, by being populated with the appropriate for each kHz frequency passive components, for the reception of the magnetic field of the East-West (E-W), North-South (N-S), and Horizontal (H) directions of the electromagnetic field, at 3 kHz or 10 kHz, respectively (left-hand side of Fig. 3). Similarly, the MHz receiver unit comprises two 1-channel MHz PCBs on which the MHz receivers are implemented, by being populated with the appropriate for each MHz frequency passive components, for the reception of the electric field at 40.455 MHz or 45.485 MHz, respectively (right-hand side of Fig. 3). Note that during the pilot operation of the MHz receivers, the 40.70 MHz and 45.95 MHz frequencies were used. Therefore, in the initial publications the specific MHz frequencies were referred to as “41 MHz” and “46 MHz”, respectively. For this reason, and since the results are not notably influenced by a slight change in the center frequency of the monitored narrowband, the “41 MHz” and “46 MHz” were retained in the published works, where the signals acquired by these receivers are analyzed, even after the final frequency selection (40.455 MHz and 45.485 MHz), [e.g., Eftaxias et al., 2001; 2004; 2008; 2018; Potirakis et al., 2011; 2012a; 2012b; 2012c; 2019a; 2022; Kapiris et al., 2004a; Karamanos et al., 2006; Papadimitriou et al., 2008; Contoyiannis et al., 2005; Eftaxias and Potirakis, 2013; Minadakis et al., 2012a; 2012b]. Note also that, based on the same kHz receiver design, 2-channel PCBs have also been developed, since in some remote telemetric stations we measure only the E-W and N-S components at 3 kHz and 10 kHz.

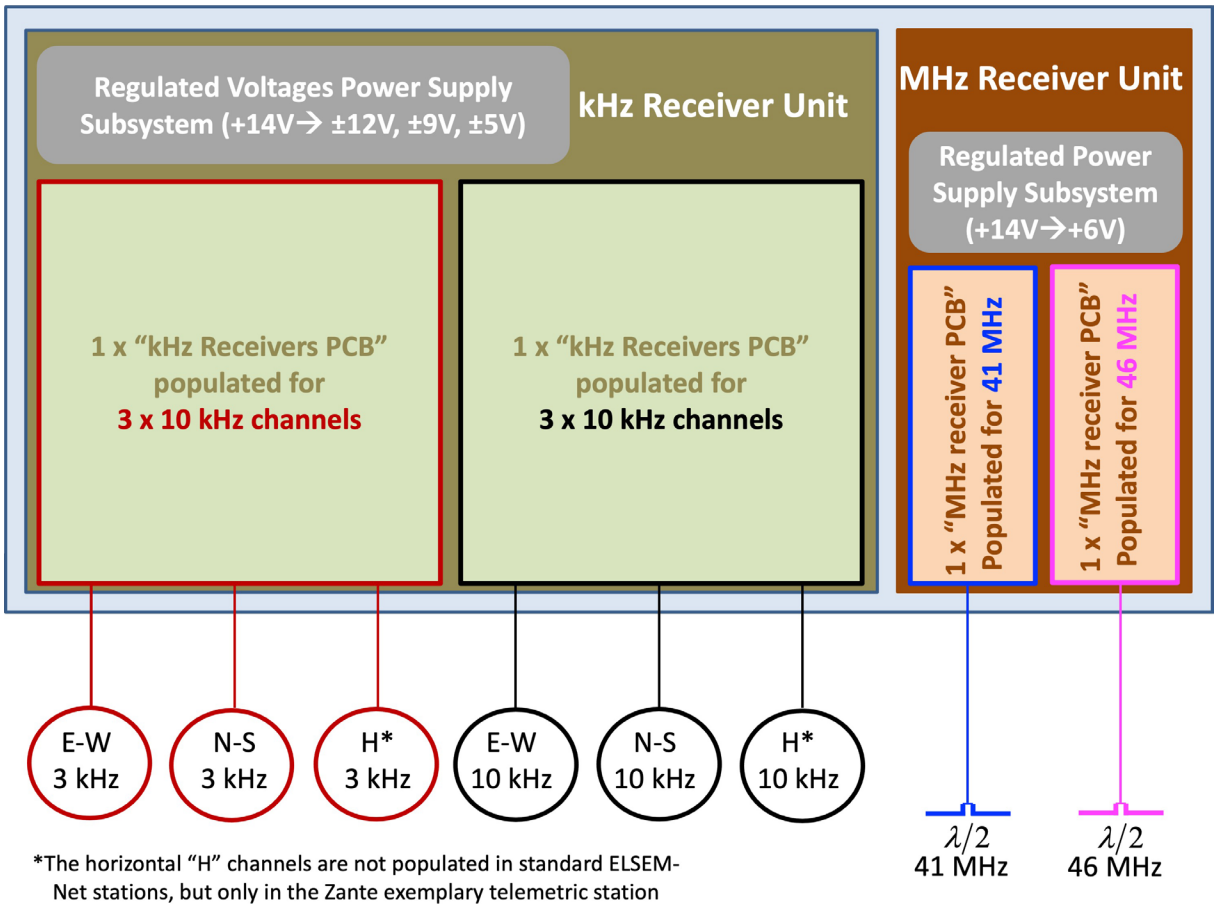

Figure 3. Block diagram of the antennas and receivers of a standard ELSEM-Net. The organization of the units on PCB level is indicated by blocks of different colors, while the associated antennas are also shown. Please cf. to the text (Sec. 3.1) for a detailed description.

The block diagram of each channel of the kHz receiver design is given in Fig. 4. The first module is a capacitor bank for the matching of the corresponding loop antenna during the initial installation, as well as during the periodic maintenance of the station where the system is used.

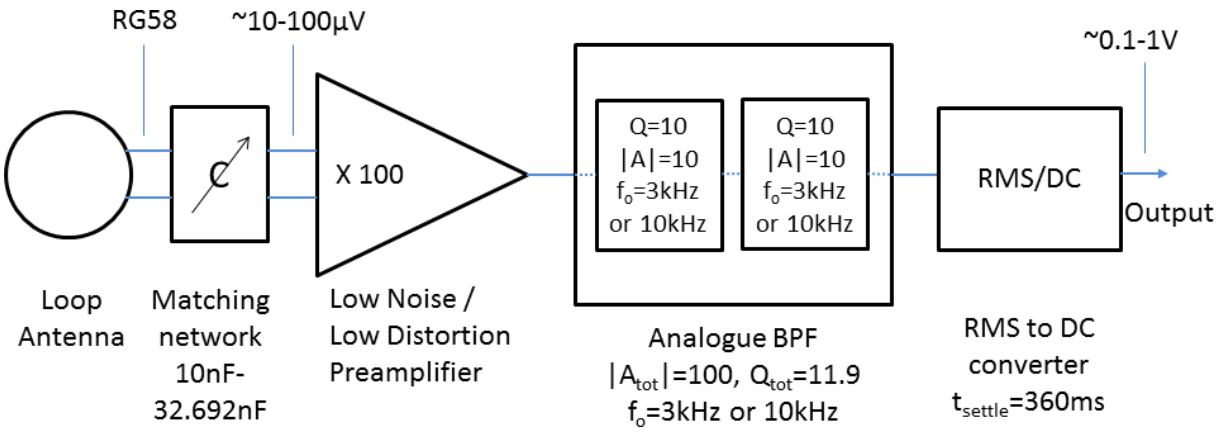

Figure 4. Block diagram each channel of the kHz receiver design. The main functional blocks along with basic characteristics information are depicted. The output of the receiver is a slowly varying signal, proportional to the root mean square (rms) value of the magnetic field strength H_{rms}. This is sent to the datalogger where it is sampled at a rate of 1 sps ($f_s = 1$ Hz).

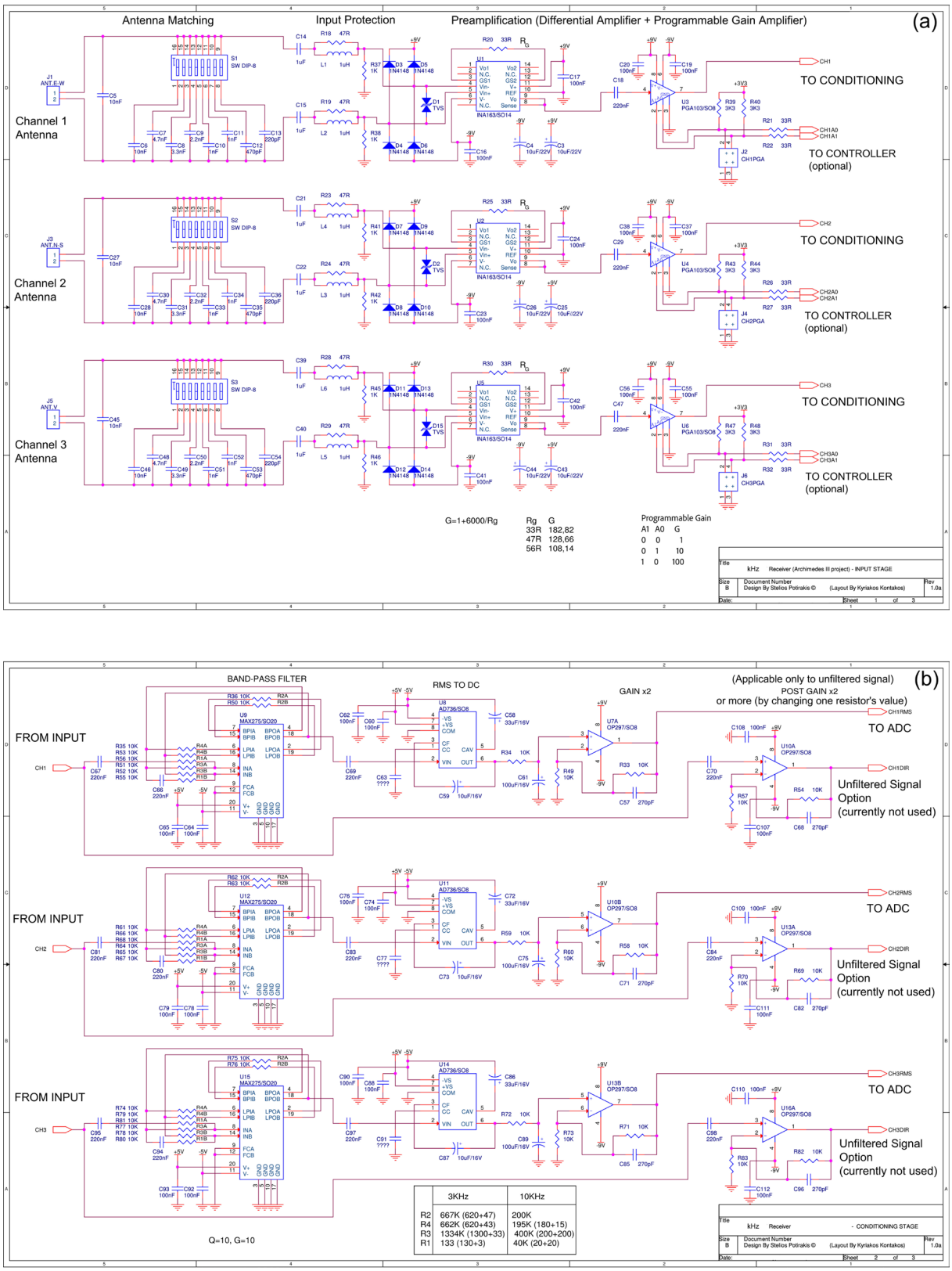

Figure 5. Latest kHz receiver design schematics: (a) Input stages, comprising antenna matching, input protection and preamplification circuits; (b) Signal conditioning stages, comprising narrowband band-pass filtering, rms-to-dc and post amplification. The receiver circuits continue from (a) to (b) as indicated by the network names and corresponding comments. The comments "TO CONDITIONING" in (a) denote signals continuing to (b), whereas the comments "FROM INPUT" denote signals coming from (a). By selecting passive component values, dip-switch positions, and using jumpers one can define whether each receiver channel will be a 3 kHz or a 10 kHz receiver, change the gain and match the corresponding antenna.

By a simple in-situ test procedure, the appropriate capacitance is selected each time. The next stage is a preamplifier with very low noise and distortion that amplifies the signal by a factor of 100 (or more). Successively, the amplified signal passes through two identical cascaded narrowband band-pass filters tuned at the frequency of interest (3 kHz or 10 kHz). Finally, the filtered signal passes through an rms (root mean square) to dc (direct current) stage to produce the slowly varying output signal. This is proportional to the rms value of the received magnetic field strength H_{rms}. The output signal is directed, as it happens for all the output signals of the receivers of our system, to an appropriate datalogger and transmission system [Koulouras et al., 2005b; Tsiriggakis et al., 2005; Tassoulas et al., 2010], where they are sampled at a rate of 1 sps ($f_s = 1$ Hz). Figure 5 shows the schematics of the latest kHz receiver design, while Fig. 6 shows typical input-output characteristic measurements for the kHz receivers. It is noted that the outputs CHxDIR (x = 1,2,3) appearing at the rightmost end of Fig. 5b are currently not used but provide the option to directly provide the original signal reaching the antennas (without any filtering or other pre-processing) to the datalogger for future experimentation. Moreover, the comments "TO ADC" appearing in Fig. 5b indicate the outputs of the receiver towards the analog to digital conversion unit of the datalogger, whereas the comments "TO CONTROLLER" in Fig. 5a indicate optional control signals that can be provided by a micro-controller to soft-set the gain instead of short-circuiting the appropriate pins of J2, J4 and J6 (using jumpers) to hard-set the gain of the programmable gain amplifiers.

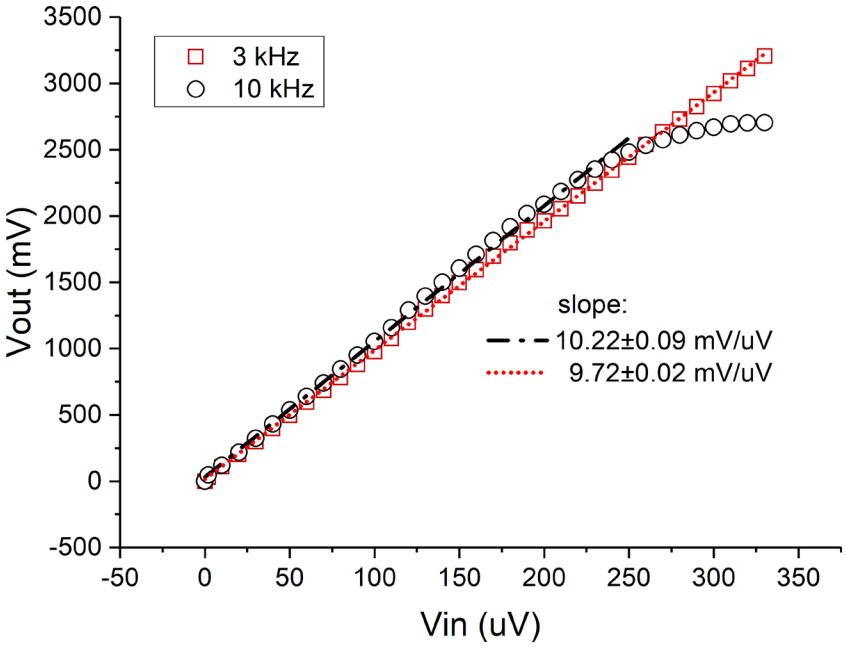

Figure 6. Example of measured input-output characteristics for two typical kHz receivers. The linear region of operation, as well as the gain slope of ~10,000 V/V can be easily identified.

The block diagram of the MHz receiver design is given in Fig. 7. This is based on a typical heterodyne receiver of a standard intermediate frequency ($IF = 455$ kHz). The low-noise/low-distortion preamplifier is succeeded by a mixer where the local oscillator frequency f_{LO} and the received frequency f_{RF} produce the IF frequency as $f_{IF} = f_{RF} - f_{LO}$. Then, all other frequencies, except f_{IF}, are filtered-out and f_{IF} passes through a pair amplifier/limiter. The useful output in our case is the received signal strength level that is estimated by the RSSI stage followed by a very low frequency first-order passive low-pass filter (cf. Fig. 7). The MHz receiver design is built around the SA605D NXP Semiconductors integrated circuit (IC), as shown in Fig. 8. Note that the specific design is ~30 years old, and as a result the specific IC is currently at "end-of-life" status, while some other key components, such as the 45.030 MHz crystals are now very difficult to find. Therefore, we are already planning to design a replacement MHz receiver soon.

As in the case of the kHz receivers the output signal is directed to an appropriate datalogger system [Koulouras et al., 2005b; Tsiriggakis et al., 2005; Tassoulas et al., 2010] where it is sampled at a rate of 1 sps ($f_s = 1$ Hz). Figure 9 shows typical input-output characteristics' measurements for the MHz receivers.

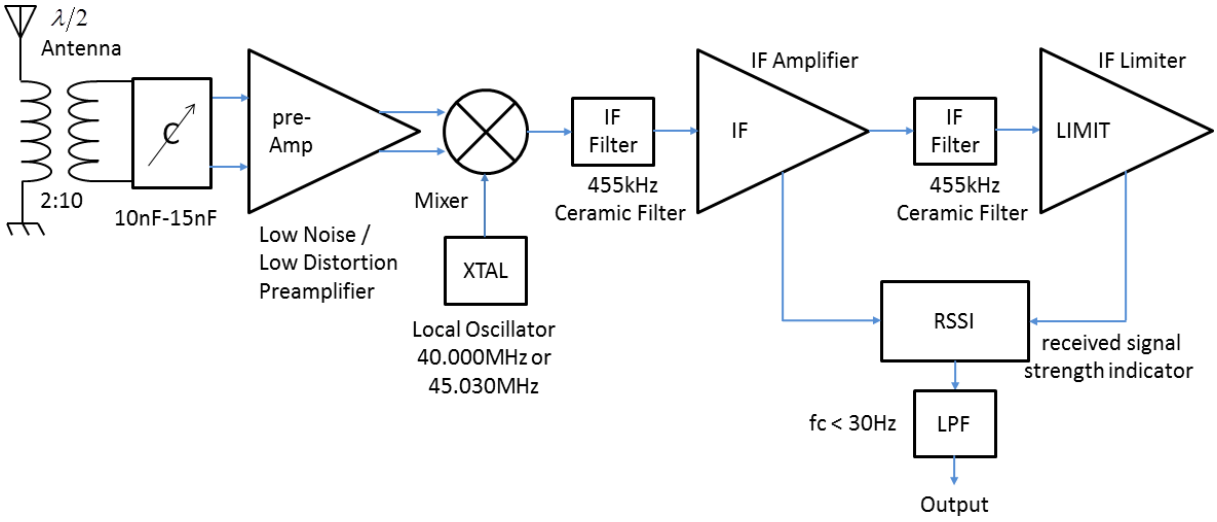

Figure 7. Block diagram of the MHz receiver design. The main functional blocks along with basic characteristics information are depicted. The output of the receiver is a slowly varying signal, proportional to the level of the electric field strength E_{rms}. This is sent to the datalogger where it is sampled at a rate of 1 sps($f_s = 1$ Hz).

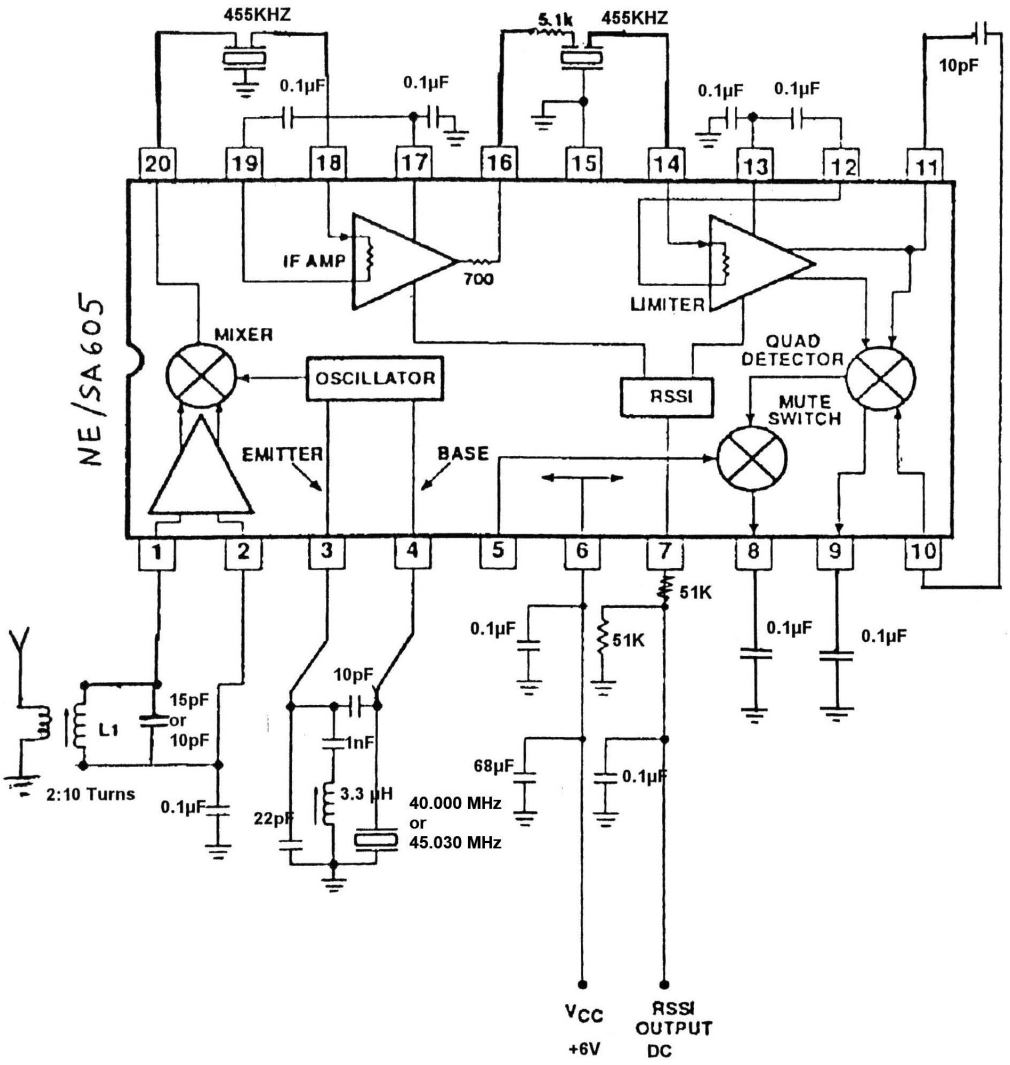

Figure 8. MHz receiver design. By changing one capacitor's value at the antenna matching circuit (15 pF or 10 pF) and the crystal (40.000 MHz or 45.030 MHz) the two MHz receivers ("41 MHz" or "46 MHz", respectively) are implemented.

The implementation of our special purpose system for the monitoring of electromagnetic field variations in the MHz and kHz bands that is based on the above-presented receivers is shown in Fig. 10. A typical installation of the complete system from one of our remote telemetric stations, along with the PCB of one of the MHz receivers (inset photo), is depicted. The presented receivers are (gradually since 1995) in operation at 11 remote telemetric stations. The cost of the 2-channel MHz receivers unit is estimated to be ~€100, while the cost of the 6-channel kHz receivers unit is estimated to be ~€500, in current commercial prices.

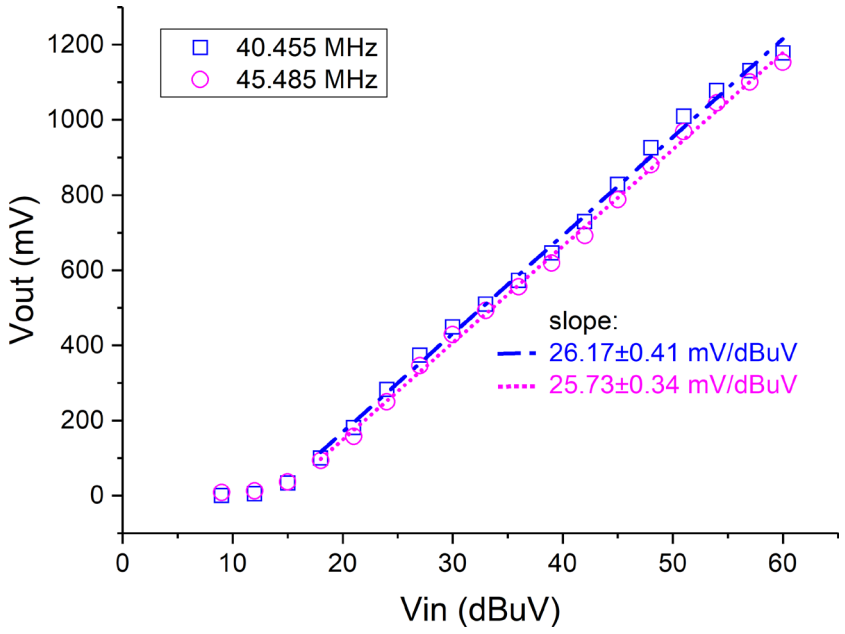

Figure 9. Measurements of the input-output characteristics for two typical MHz receivers. The linear region of operation, as well as the gain slope of ~26 mV/dBuV can be easily identified.

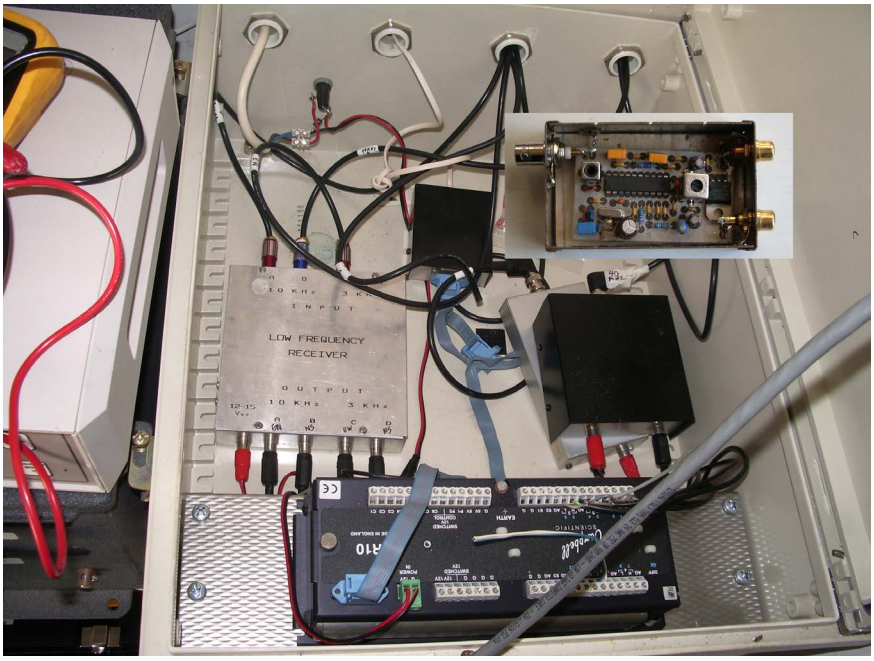

Figure 10. A typical installation of ELSEM-Net remote telemetric station instrumentation (receivers along with one of the employed dataloggers) at Archangelos, Rhodes Island (36.2135° N, 28.1212° E), station code "A". The inset photo depicts the PCB of a MHz receiver unit.

3.2 Antennas Design and Implementation

For the MHz receivers, two standard $\lambda/2$ dipole antennas [Kraus and Marhefka, 2002] were designed for the reception of the variations of the electric field at the 2 distinct frequencies mentioned above, namely at 40.455 MHz and 45.485 MHz. These antennas were manufactured using two co-linear $\lambda/4$ aluminum rod strains and are connected to a RG58, 50 Ohm, feeding cable via an appropriate coaxial (RG58) matching balun of appropriate length. Table 2 summarizes the specifications of the dipole antennas parts.

Frequency (MHz)	Wave-length λ (m)	Aluminum rod length $= 0{,}95 \cdot \lambda/4$ (m)	Coaxial Balun length $= 0{,}66 \cdot \lambda/4$ (m)
40.455	7.42	1.76	1.22
45.485	6.60	1.57	1.09

Table 2. Dipole antennas construction / functional characteristics. Balun shortening (velocity) factor of RG58 (0.66) has been taken into account in balun design. In case another coaxial cable is used its velocity factor should be used instead.

The rms value of the voltage V_{rms} induced by an incoming E-field with a polarization that is collinear to the axis of the dipole and with an angle of arrival that is perpendicular to the axis of the dipole, is calculated by Eq. (1) [Kraus and Marhefka, 2002]:

$$V_{rms} = \frac{E_{rms} \cdot \lambda}{\pi}, \tag{1}$$

where E_{rms} is the rms value of the electric field strength and λ denotes the wavelength.

The use of $\lambda/2$ dipole antennas for the reception of the variations of the geo-electromagnetic field at the kHz band is prohibitive due to the excessive dipole lengths required (50 km and 15 km for 3 kHz and 10 kHz, respectively). Therefore, for the sensing of the electromagnetic variations at the kHz band, two standard small loop antennas [Volakis, 2007] tuned at 3 kHz and 10 kHz, respectively, were designed. These low-frequency small loop antennas are usually referred to as "magnetic loops" to denote that they are sensitive to magnetic field variations. Table 3 summarizes the construction and functional characteristics of the designed antennas.

These loop antennas are indeed "small" since their perimeter is much smaller compared to the wavelength and, thus, the magnitude current spatial distribution may be considered to be a constant number [Balanis, 2005]. For small loop antennas it can be shown that the rms value of the induced voltage V_{rms} is calculated using Eq. (2) or equivalently by Eq. (3) [Carr and Hippisle, 2012]:

$$V_{rms} = \frac{2\pi A N E_{rms} Q \cos\theta}{\lambda}, \tag{2}$$

or

$$V_{rms} = \frac{2\pi A N (c\mu_0\mu_r H_{rms}) Q \cos\theta}{\lambda}, \tag{3}$$

where A is the total area of the antenna, N is the number of revolutions of the winding wire, Q is the quality factor of the antenna, E_{rms} and H_{rms} are the rms values of the electric and magnetic field strength, respectively, at the

Parameter	Value for 3 kHz antenna	Value for 10 kHz antenna
Frequency (kHz)	3	10
Q	12.04	12.16
R_{in} (Ohm)	149.6	44.4
L (H)	0.0956	0.0086
C (pF)	29,475.0	29,475.0
Perpendicular eff. Height h_e (m)	0.10	0.10
Antenna diameter D (m)	1.0	1.0
Area A (m^2)	0.785	0.785
Wire (copper) diameter d (mm)	0.28	0.28
N (revolutions)	168.5	50.0

Table 3. Loop antennas construction / functional characteristics.

center of the antenna, λ is the wavelength, and θ is the angle between the antenna plane normal and the magnetic field lines; c is the speed of light, μ_0 is the permeability of vacuum ($4\pi 10^{-7}$ H/m), and μ_r is the relative permeability of the medium (for the air $\mu_r \approx 1$). We usually define the effective height $h_e = (2\pi ANQ \cos\theta)/\lambda$ measured in (m), as a measure of the sensitivity of the loop antenna.

Figure 11. A typical ELSEM-Net remote telemetric station antennas installation at Neapoli, Crete Island (35.2613° N, 25.6103° E), station code "E". Left mast: the two 10 kHz small loop antennas (black); middle mast: the two 3 kHz small loop antennas (red); right mast (top): the 46 MHz $\lambda/2$ dipole antenna; right mast (bottom): the 41 MHz $\lambda/2$ dipole antenna.

Both the $\lambda/2$ dipole and loop antennas have been implemented and are in operation (gradually since 1995) at 11 remote telemetric stations for the measurement of electromagnetic field variations and the detection of FEME/FEMR. A typical antennas installation of an ELSEM-Net station is shown in Fig. 11. The cost for the construction of the dipole and loop antennas in current commercial prices is ~€40 and ~€100 per antenna, respectively.

3.3 A new "Single-Board Computer – Expansion Board" Datalogger

ELSEM-Net has been using for many years (> 20 years) two kinds of dataloggers; in each station either the commercially available Campbell CR10X (https://www.campbellsci.com/cr10x) (last accessed on 14 May 2023), or the specifically designed for the needs of ELSEM-Net "Mega Datalogger" [Koulouras et al., 2005a; 2014] is used. However, on the one hand, both of them are already outdated, with no support both in terms of SW updates and in terms of HW maintenance/repairs, while, on the other hand, the situation in network availability (both wired and wireless), internet access, and the data volume transfer capabilities have vastly changed during the last 20 years rendering simpler and much more cost-effective solutions feasible. Based on these grounds, it has become obvious that a new datalogger solution is necessary for the progressive replacement of the legacy dataloggers of ELSEM-Net.

The MHz and kHz receivers of ELSEM-Net are designed to output a voltage signal in the range of 0 V-2 V. These signals must in the next stage be digitized, stored, and finally transferred from each receiving station to a central data server, in our case a network-attached storage (NAS) device (see Section 4.2). For this purpose, a new datalogger has been designed based on a Raspberry Pi single-board computer (Raspberry Pi 4 Model B/4GB, (https://www.raspberrypi.com/products/raspberry-pi-4-model-b/) (last accessed on 14 May 2023), equipped with the "Waveshare Raspberry Pi High-Precision AD/DA Expansion Board" (https://www.waveshare.com/product/raspberry-pi/hats/ad-da-audio-sensors/high-precision-ad-da-board.htm) (last accessed on 14 May 2023) (see Fig. 12), since there is no high precision analog to digital conversion (A/D) capabilities on the Pi GPIO interface. Note that, the expansion board's digital to analog conversion (D/A) part is currently not used. The Raspberry Pi platform was chosen because of its impressive capabilities, the availability of many expansion boards, the availability of a wide variety of open-access software, and its low price. However, the same datalogger setup can easily be implemented by other Linux-operated single-board computers of similar capabilities, such as Banana Pi, Orange Pi, Cherry Pi, AML-S905X-CC (Le Potato), NanoPi M1 plus Allwinner H3 etc., while the above-mentioned expansion board can easily be reproduced or replaced by any other A/D expansion board of equivalent or better features.

The proposed datalogger setup can log up to 8 analog single-ended or 4 differential channels. Its precision is 24-bit and is based on the ADS1256 A/D IC. The sampling rate is adjustable from 1 sps to 30 ksps. A standard ELSEM-Net datalogger is currently using 6 of the 8 available single-ended analog inputs to convert the voltage output signals of the standard 6 receivers to digital signals, using a sample rate of 1 sps ($f_s = 1$ Hz). An appropriate program has been written in Python language that captures signals' amplitudes of all local receivers connected to the datalogger and locally stores them in daily files of recordings, while, by an appropriate script, all previous day's daily files are once per day transferred to the NAS device from each datalogger (see Fig. 12 and Section 4.2 for information about the data files format and the data management scheme). The local storage of daily files of recordings is done on an external USB storage device for data security reasons (see Fig. 13).

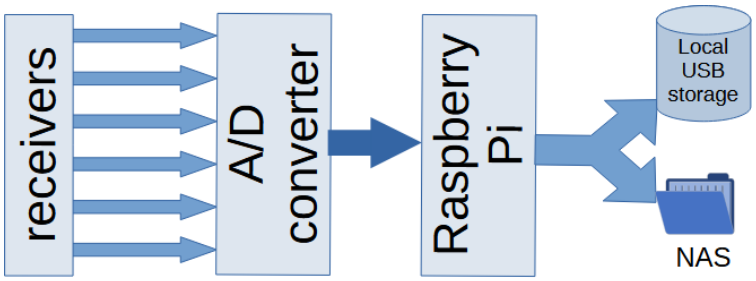

Figure 12. On every station six receivers deliver their outputs (voltage amplitude) to an A/D converter which captures the signals, and a Raspberry Pi-type single-board computer process these data and stores them locally. Every 24 hours two daily files (in two different formats) from every station are sent to a NAS for storage and further processing.

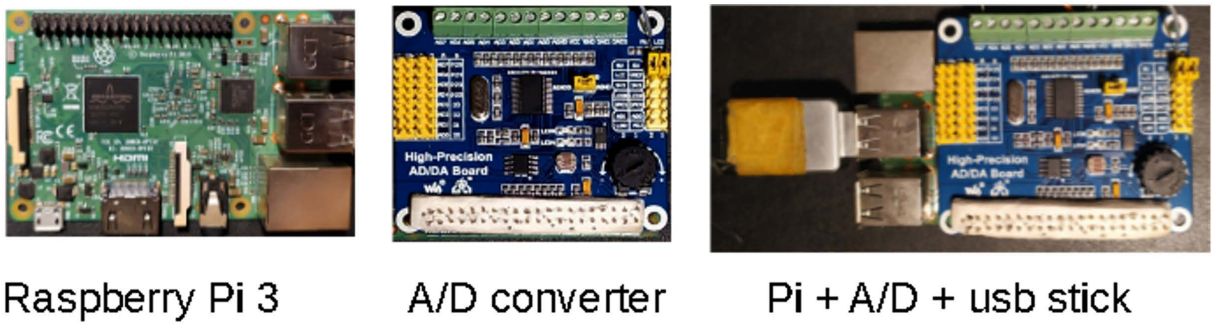

Figure 13. The new ELSEM-Net advanced and low-cost datalogger consists of a Raspberry Pi-type single-board computer, a high-precision A/D expansion board designed for Pi. An external USB storage device is added to the design for the safe keeping of data in case of failure of computer's SD-type RAM.

Raspberry Pi does not have a real-time clock (RTC) system on board, whereas accurate time is mandatory for the constant synchronization of all the ELSEM-Net stations, since all recordings are timestamped. Therefore, all new dataloggers are equipped with an external RTC expansion board based on the DS3231 IC, as well as an external USB GPS receiver connected to the Raspberry Pi. All communications of the new dataloggers are conducted through a private virtual network (VPN) (see Section 4.2). There is a NAS device in the VPN, which is uninterruptedly connected to the internet, acting as a network time protocol (NTP) server on which all dataloggers are synchronized. The GPS receiver and the RTC are filling the accurate time determination gap between the wake-up from power failure and the connection to VPN or during any communication failures. RTC has been used as a backup solution, in case of a GPS receiver failure. An appropriate SW is written in Python to ensure accurate synchronization to real time for the datalogger at all times using the above-mentioned three timestamp inputs and considering the following hierarchy: (i) NTP, (ii) GPS, (iii) RTC (see Fig. 14).

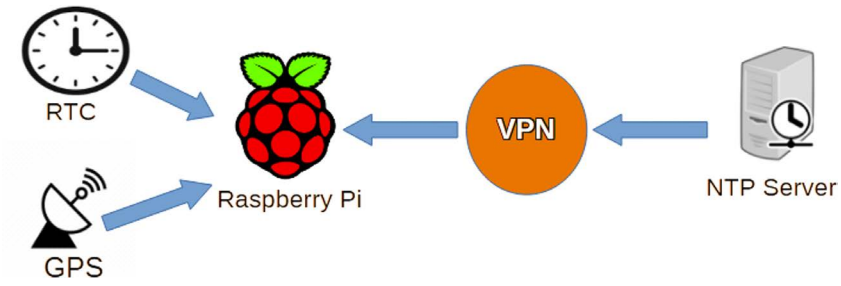

Figure 14. Three ways to synchronize a Raspberry Pi to real time. External RTC, GPS receiver, and through the network from an NTP server.

To check the new datalogger's performance, an experimental station was installed in a mountainous region close to UniWA according to the setup presented in Fig. 15. As shown in Fig. 15, a legacy Campbell CR10X datalogger and a new Raspberry Pi-based datalogger were recording the same signals in parallel. After an experimental operation of 3 months, the specific setup proved that the new datalogger not only outperforms the legacy datalogger in measurement accuracy, as shown in Figs. 16-18, but is also consumes much less power, which is also very important in remote installations without connection to the power network. Specifically, the recordings of the two dataloggers are in general in very good agreement as Fig. 16 shows, although a slight time shift is observed (see Fig. 16 inset). The observed time shift was found to be due to the poorly synchronized internal clock of the legacy datalogger (see Fig. 17). If one shifts the two recordings to compensate for the clock difference, and rounds the Raspberry Pi-based datalogger recordings to the accuracy of measurement of the legacy one since the former ones are of much higher accuracy than the latter ones (24 bits vs. 13 bits), the two recordings are practically identical, especially for low voltage amplitudes (input < 700 mV).

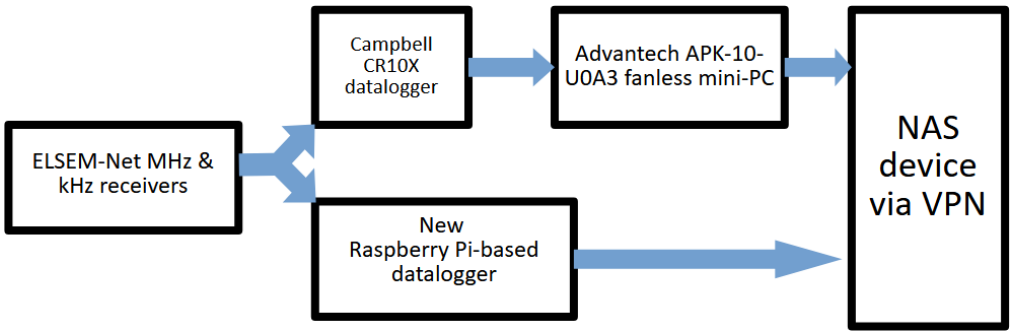

Figure 15. The six ELSEM-Net receivers' outputs are connected in parallel to a legacy datalogger Campbell CR10X and the new Raspberry Pi datalogger in order to evaluate the performance of the new datalogger.

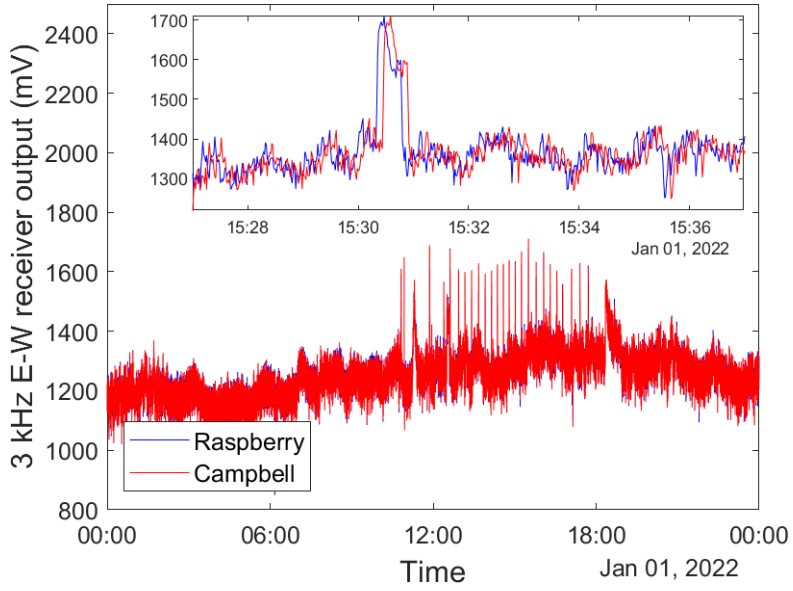

Figure 16. The recordings of the 3 kHz E-W receiver's signal on 01/01/2022 by the legacy datalogger Campbell CR10X and the new Raspberry Pi datalogger (presented on a common time axis), where a slight shift time is observed (see inset). This time shift is due to the poorly synchronized internal clock of the legacy datalogger (see also Fig. 17).

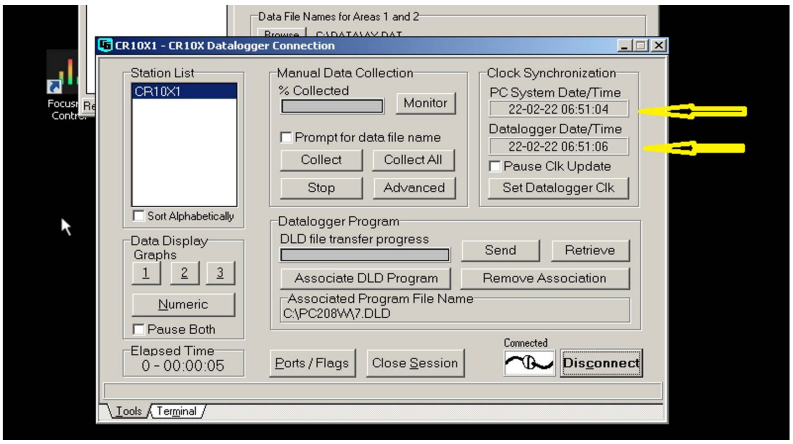

Figure 17. PC208W SW (Campbell Scientific proprietary software) report window. The yellow arrows indicate the poor synchronization of the internal clock of the used Campbell CR10X datalogger to the clock of the Advantech APK-10-U0A3 fanless mini-PC (which was synchronized to the same NTP server as the new Raspberry Pi-based datalogger).

In order to investigate what happens for higher input values, we applied voltage ranging from 0 mV to 2800 mV from an external high-stability DC power supply in parallel to one input of the Campbell CR10X and one input of the Raspberry Pi-based datalogger, while in parallel measuring the input voltage by a high-accuracy bench multimeter. The results are depicted in Fig. 18, showing that the difference between the applied and recorded voltage for the new Raspberry Pi-based datalogger was very low, $< \pm 10$ mV for the whole range of the input voltage. On the other hand, the Campbell CR10X, although showed excellent performance up to 700 mV, for higher input values the difference between input and recorded value was worse than that of the Raspberry Pi-based datalogger, and monotonically increasing, reaching up to 85 mV difference for 2800 mV input. From Fig. 18, it is clear that, in contrast to the legacy datalogger, the Raspberry Pi-based datalogger curve is well approximated by a linear function, which renders its calibration far easier, just by a linear trend compensation.

Finally, the Raspberry Pi-based datalogger is consuming only 0.9 W when acquiring data and works at 20% of the computing power, while in the 100% computing power state its consumption is only 3 W. On the other hand, the legacy datalogger setup (Campbell CR10X and Advantech APK-10-U0A3 fanless mini-PC running Campbell Scientific proprietary SW) consumes ~36 W during data acquisition.

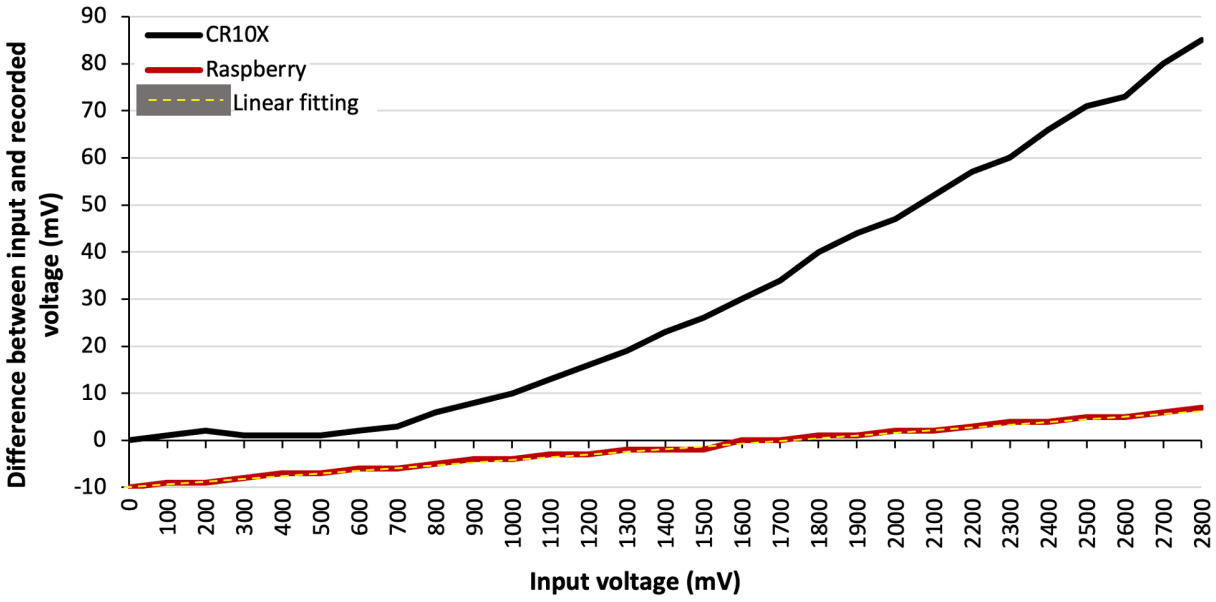

Figure 18. Difference between the applied and recorded voltage vs the applied voltage for the Campbell CR10X and the new Raspberry Pi-based datalogger. The new Raspberry Pi-based datalogger presents a very low, $< \pm 10$ mV, difference for the whole range of the input voltage, while the legacy Campbell CR10X presents excellent performance up to 700 mV, but worse than that of the Raspberry Pi-based datalogger for higher input values. The new datalogger curve presents a linear trend, unlike the legacy one.

4. ELSEM-Net Software

The key information concerning the software (SW) used for the ELSEM-Net is presented in the following Sections. Specifically, Section 4.1 presents the website developed for ELSEM-Net and Section 4.2 presents data management issues.

4.1 The website: A Collaboration Platform

ELSEM-Net website (http://elsem-net.uniwa.gr) (last accessed on 14 May 2023) is a solution created to communicate and support the research related to the specific network of ground-based telemetric stations for the monitoring of FEME/FEMR in Greece (see Fig. 19). It serves as the central information hub of the general information

regarding ELSEM-Net, such as geographical allocation via interactive maps, photos and recent recordings of each station, status per station, research team, research results, relevant publications, news, and current activities. Moreover, it is also a platform which the researchers of ELSEM-Net can use to have easy and versatile access, for both visualization and download, to decades of signals recorded by the telemetric stations, preliminary (automated) analysis results, etc. (see Fig. 20). Specifically, the website consists of a public section that anyone can access, an approved-members-only section where all ELSEM-Net researchers, as well as authorized collaborating researchers, can access via login, and the admin panel via a login which is there as a GUI (Graphics User Interface) for detailed information stored in the associated database. Each page corresponds to the equivalent admin panel where someone with access can add or remove content.

Multiple technologies are used in order to make a website work as expected, especially now that it needs to be displayed in multiple devices. The frame of the website is constructed in Hyper Text Markup Language (HTML) which is the standard markup language used when displaying documents on a web browser. With the help of Cascading Style Sheets (CSS) this document is presented in a way that a user can easily navigate. When using CSS there are

Figure 19. Screen-shot of the ELSEM-Net home page. Only part of the home page is presented; more information on the motivation of this research, the network and stations' structure, and key research results are available by scrolling down.

Figure 20. Screen-shot of the ELSEM-Net "Data" page, which is available only to ELSEM-Net researchers, as well as authorized collaborating researchers. Only part of the "Data" page that fits the browser window is presented. From this page one can have access to the recorded data, as well as preliminary analysis results, both for visualization and download.

frameworks that reduce the code that needs to be written, improving functionality, and provide useful templates for the website and Bootstrap was the open-source framework of choice, due to its responsive, mobile-first, approach. JavaScript is a language that provides the functionality of the website, such as what each button does and much more complex functionalities. On top of the website functionality, Leaflet open-source library was used for maps, and Highcharts for the time series plots. Since the website needs to be dynamically produced, PHP was used. It provides logic and through certain conditions, produces the content that the user needs to see. Some examples are: populating a table with stations or showing news in their individual templates. The ELSEM-Net website is hosted in a virtual machine server, while all information appearing in the website is stored in a database, physically hosted in a network-attached storage (NAS) device. Both the virtual machine of the server and the NAS are installed in the UniWA and is part of the infrastructure of the Electronics and Computer Technologies Lab (ECTLab, http://ectlab.eee.uniwa.gr/index.php/en) (last accessed on 14 May 2023).

MySQL was chosen as the SQL language that enables to retrieve, transform and delete data through the use of queries because the used NAS device uses MariaDB as an open-source relational database, which in turn uses MySQL. This database management system offers a secure way to handle data, as it can set permissions to users, denying the request to delete or overwrite the data. Since the database stores all the information that is needed for the proper functionality of the website, many different tables are accessed depending on what the user requests while browsing. If a user for example opens the "Stations" page, a request is sent to the database and the database returns a list of all available stations along with their information (see Fig. 21).

(a)

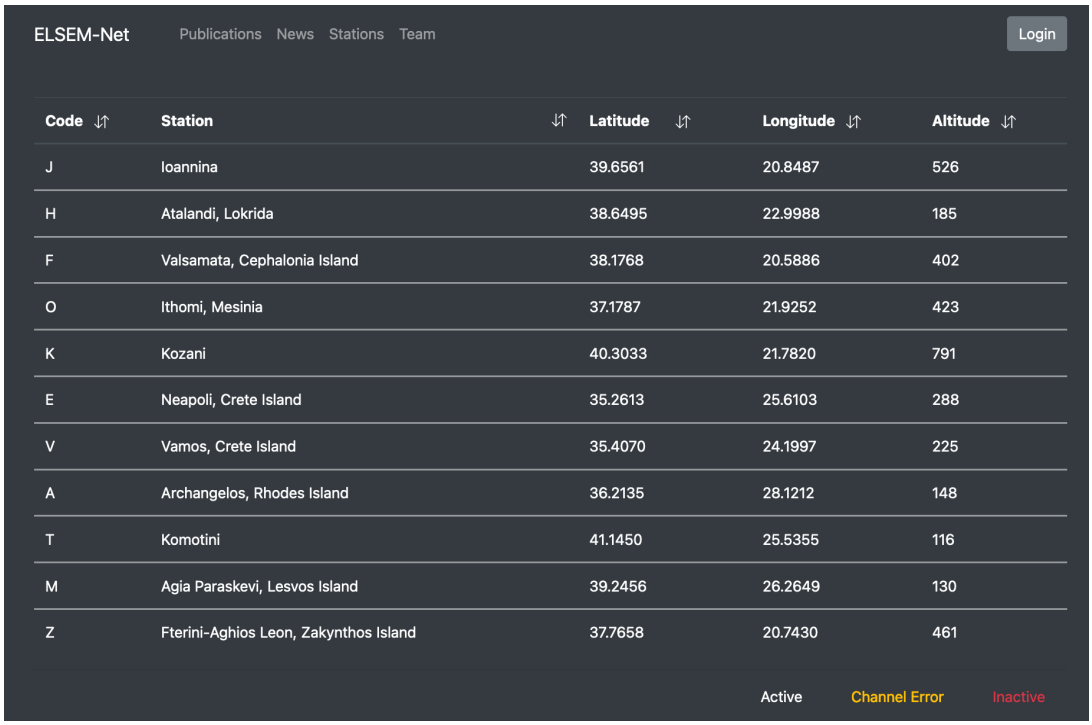

Code	Station	Latitude	Longitude	Altitude
J	Ioannina	39.6561	20.8487	526
H	Atalandi, Lokrida	38.6495	22.9988	185
F	Valsamata, Cephalonia Island	38.1768	20.5886	402
O	Ithomi, Mesinia	37.1787	21.9252	423
K	Kozani	40.3033	21.7820	791
E	Neapoli, Crete Island	35.2613	25.6103	288
V	Vamos, Crete Island	35.4070	24.1997	225
A	Archangelos, Rhodes Island	36.2135	28.1212	148
T	Komotini	41.1450	25.5355	116
M	Agia Paraskevi, Lesvos Island	39.2456	26.2649	130
Z	Fterini-Aghios Leon, Zakynthos Island	37.7658	20.7430	461

Active Channel Error Inactive

(b)

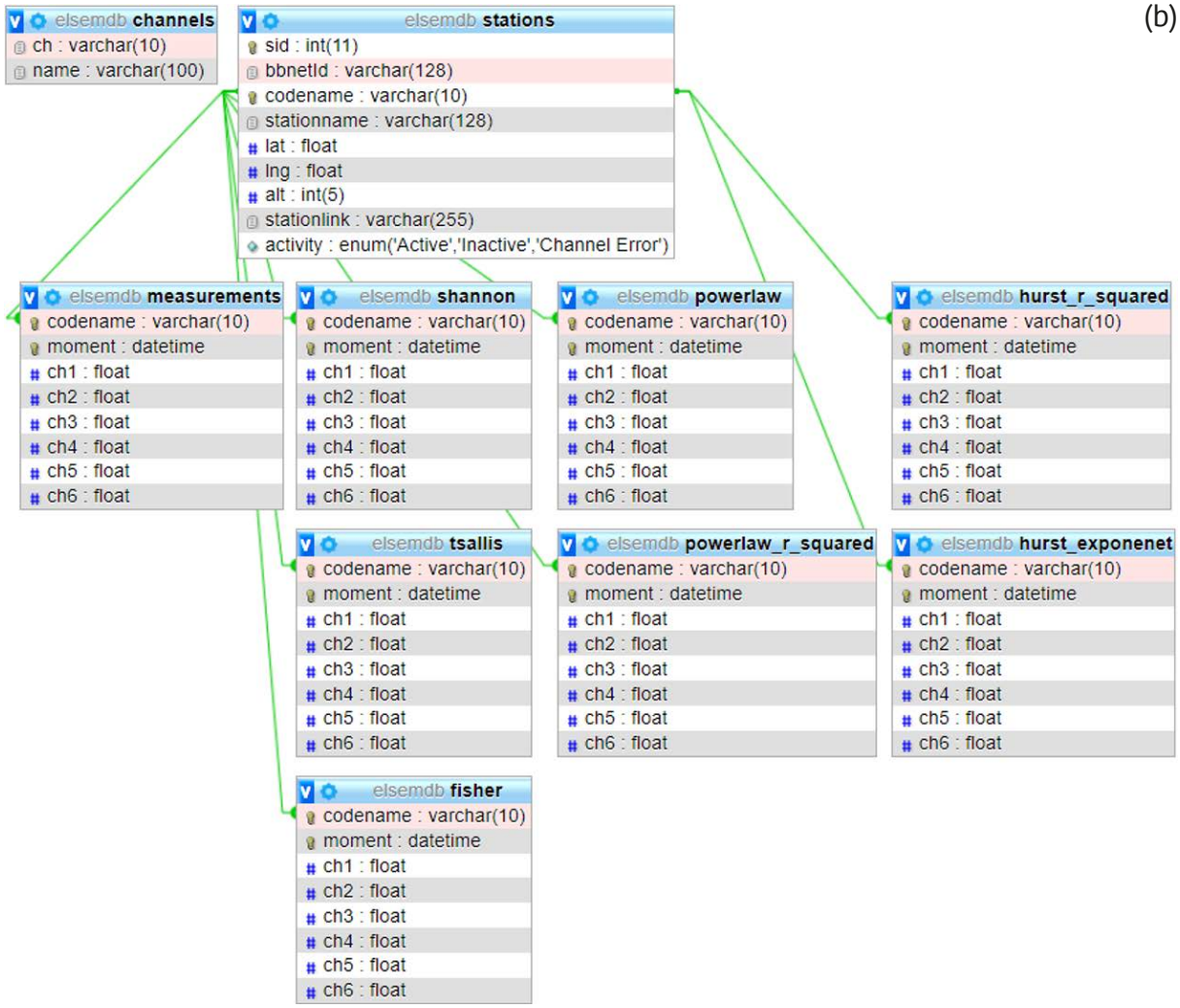

Figure 21. (a) Screenshot of the ELSEM-Net "Stations" page (only part of the "Stations" page is presented). (b) Database information requested by the website when one opens the Stations page.

4.2 Data Management

Currently, a hybrid data management scheme is adopted to serve both legacy and new dataloggers, until all the legacy dataloggers of the network are replaced by the new ones (see Section 3.3).

Concerning the management of the legacy dataloggers' data, each station's data are first automatically hourly transmitted to a dedicated server hosted in a virtual machine of the Institute of Geodynamics of the National Observatory of Athens (NOA/IG), using a communications and data transfer scheme implemented by custom SW modules running both at the legacy dataloggers and the server of NOA/IG [Kefalas et al., 2011]. Each legacy hourly

(a)

Day of Year	*HHMM*	*SS.MS*	*Channel 1*	*Channel 2*	*Channel 3*	*Channel 4*	*Channel 5*	*Channel 6*	*Battery*
02+0306.	03+0300.	04+00.00	05+926.6	06+06.17	07+207.3	08+126.1	09+215.0	10+379.4	11+11.93
02+0306.	03+0300.	04+01.00	05+930.2	06+04.93	07+187.3	08+144.4	09+214.2	10+358.6	11+11.93
02+0306.	03+0300.	04+02.00	05+930.2	06+04.93	07+187.3	08+144.4	09+214.2	10+358.6	11+11.93
02+0306.	03+0300.	04+03.00	05+930.2	06+04.93	07+187.3	08+144.4	09+214.2	10+358.6	11+11.93

(b)

No meaning	*Day of Year*	*HHMM*	*SS.MS*	*Channel 1*	*Channel 2*	*Channel 3*	*Channel 4*	*Channel 5*	*Channel 6*	*Battery*
102,	306.,	0000.,	59.00,	905.8,	04.93,	180.0,	121.2,	214.5,	370.9,	11.93
102,	306.,	0001.,	00.00,	926.6,	06.17,	207.3,	126.1,	215.0,	379.4,	11.93
102,	306.,	0001.,	01.00,	930.2,	04.93,	187.3,	144.4,	214.2,	358.6,	11.93

(c)

A2016068

codename	moment	ch1	ch2	ch3	ch4	ch5	ch6
A	2016-03-08 00:00:00	4.93	982.7	202.2	335.4	630.1	511.7
A	2016-03-08 00:00:01	4.93	979.0	202.2	339.1	633.8	519.1
A	2016-03-08 00:00:02	4.93	1000.0	197.3	332.9	632.5	521.6
A	2016-03-08 00:00:03	4.93	1001.0	189.9	329.2	627.6	584.4
A	2016-03-08 00:00:04	4.93	981.5	192.3	335.4	628.8	536.4

(d)

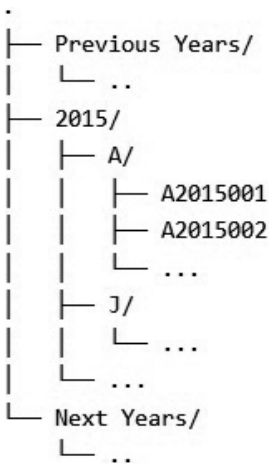

Figure 22. (a) A few lines of a legacy hourly file (day 306, 03:00:00-03:00:03), where data are stored in a tab-separated format. (b) A few lines of a legacy daily file (day 306, 00:00:59-00:01:01), where data are stored in a comma-separated format. (c) A few lines of a new .csv daily file (data recorded at the station with codename "A" during the day 68 of 2016, 00:00:00-00:00:04), the filename is shown on top of the data and follows the legacy daily files naming convention. (d) The folder structure for storage of daily files, organized first by year and then by station.

file is an ASCII text file with file extension ".dat", named according to the following naming convention: Each name consists of eight alphanumeric characters, the first one is the letter representing the codename of the station, the next three represent the day number (day of the year), and the last four represent the hour of the day. For example, the file "O3540300.dat", contains the data of the 354th day (of the specific year), from 03:00:00 to 03:59:59 UT, recorded by the station with codename "O" (see Fig. 22a for a sample of the data contained in an hourly file). At the NOA/IG server, all the received hourly files of each station produced during a specific day are stored in a single folder, named according to the following naming convention: each folder name consists of four alphanumeric characters, the first one being the letter representing the codename of the station and the next three representing the day number. For example, the folder "A306" contains all hourly files of the 306th day (of the specific year), containing data recorded by the station with codename "A". Each of these folders' contents are automatically daily added to one .zip file (one .zip file per station is produced), named after the corresponding folder's name (e.g., "A306.zip") and later on all previous day's .zip files are synchronized to the NAS device located at UniWA. At the NAS, each .zip file is unzipped and all the hourly files contained are used to automatically produce a corresponding legacy daily ASCII text file with the file extension ".dat", named according to the following naming convention: Each name consists of eight alphanumeric characters, the first one is the letter representing the codename of the station, the next four represent the year and the last three represent the day number (day of the year). For example, the file "F2022168.dat", contains the data of the 168th day of the year 2022, recorded by the station with the codename "F" (see Fig. 22b for a sample of the data contained in a legacy daily file). Then, the legacy daily files are used to automatically (by an appropriate Python script) produce daily files in a new the new CSV format (see Fig. 22c), which is appropriate for direct access by many contemporary visualization and analysis SWs, as well as for direct import to databases. Finally, both kinds of daily files (legacy .dat and new .csv) are organized in folders according to the scheme presented in Fig. 22d.

Concerning the management of the new dataloggers' data, all new dataloggers store locally only daily files both of the legacy .dat and new .csv formats (see Figs. 22b and 22c) and along with the NAS device are members of a private virtual network (VPN), implemented using the "WireGuard" communication protocol, a free and open-source SW that uses state-of-the-art cryptography (https://www.wireguard.com) (last accessed on 14 May 2023). Once per day, the previous day's daily files, both legacy .dat and new .csv, from all new dataloggers are transferred to the NAS device using the "rsync" open-source utility available for Linux (https://rsync.samba.org) (last accessed on 14 May 2023), and organized in folders according to the scheme presented in Fig. 22d.

5. Analysis of Fracture-Induced Electromagnetic Emissions

As an example of the analysis performed on ELSEM-Net recordings, in the following we present the analysis of MHz signals recorded in different stations of ELSEM-Net prior to three significant EQs that recently occurred in Greece. The presented analysis aims at the reveal of criticality indications prior to each one of these EQs, using a recently introduced time series analysis method that relies on wavelet analysis to achieve a coarse-graining that permits the extraction of dynamics information from noisy data [Contoyiannis et al., 2020]. Indeed a few days before each one of the studied EQs criticality was found in the MHz recordings of a relatively close-in-distance ELSEM-Net station. Section 5.1 provides information about the studied EQs, the analysis method is presented in Section 5.2, while Section 5.3 presents the analysis results.

5.1 Recent Earthquakes Information

As already mentioned in the Introduction Section of this article, in this subsection we study three recent significant EQs ($M_W \geq 5.9$) that occurred in 2020 and 2023 in Greece. All the necessary details of each of one of the three EQs have been acquired from European-Mediterranean Seismological Centre, EMSC-CSEM (https://www.emsc-csem.org/, last accessed on 14 May 2023), and are given in Table 4. Based on the magnitude of the EQ, the critical radius ($R_{cr} = 10^{0.44 \cdot M_W - 0.78}$) has been calculated in km for each one of the studied EQs [Bowman et al., 1998]. Figure 23 shows a satellite image of the part of the area of the southeastern Mediterranean that includes Greece, in which the locations of all ELSEM-Net stations are marked. Each one of the three studied EQs' epicenter is shown on the map along with its date of occurrence and magnitude. In addition, the "critical zone" as defined by the critical radius of each EQ is also shown on the map. Note that, in all studied cases the corresponding critical zone includes

land parts. This fact, according to the reasoning presented in detail in [Eftaxias and Potirakis, 2013; Eftaxias et al., 2018], renders the hypothesis that FEME/FEMR is launched to the atmosphere reasonable, and thus FEME/FEMR can be detectable by ELSEM-Net stations. It is also worth mentioning that the analyzed signals were recorded by the ELSEM-Net station closest to the epicenter of each studied EQ (see Section 5.3). Especially for the case of the 2020 Crete EQ, it has to be clarified that station "E", which is the closest one, was temporarily malfunctioning, so we used the recordings of the next closest station (station "V"), also located on Crete Island.

EQ herein referred to as	Epicenter location	Time of occurrence (UT)	Magnitude (M_W)	Depth (km)	Latitude (° N)	Longitude (° E)	Critical radius (km)
2020 Crete EQ	97 km S of Ierapetra, Crete Island	02/05/2020 12:51:05.4	6.6	10	34.14	25.70	133
2020 Samos EQ	18 km NNE of Karlovasi, Samos Island	30/10/2020 11:51:25.7	7	10	37.91	26.84	200
2023 Rhodes EQ	69 km SE of Lindos, Rhodes Island	25/01/2023 12:37:06.4	5.9	35	35.75	28.54	65.46

Table 4. Information about the EQs under study as taken from EMSC-CSEM.

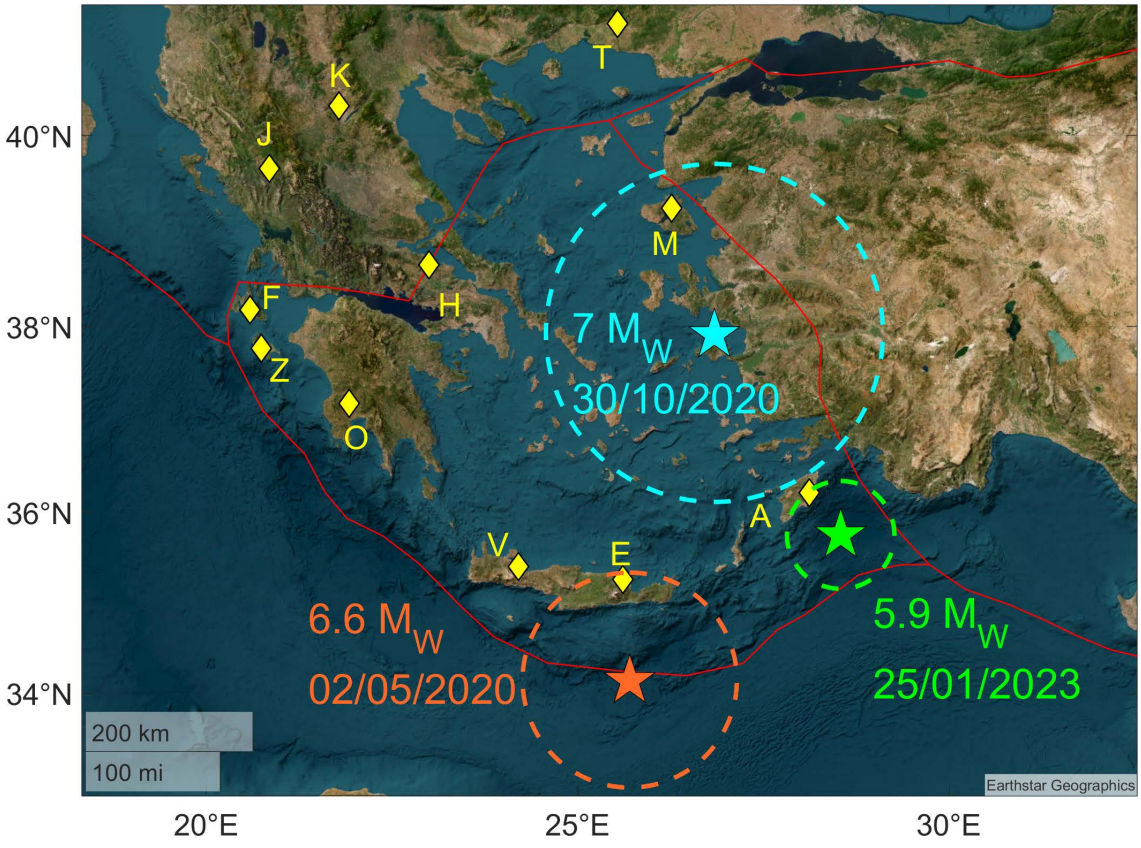

Figure 23. Satellite image of a part of the area of the southeastern Mediterranean that includes Greece. ELSEM-Net stations are indicated by yellow diamonds (station codes are also shown). The three pentagrams (cyan, light green and orange) depict the epicenter locations of the three studied EQs, whereas the dates of occurrence and magnitudes are also shown. Moreover, the circles (dashed circumferences), centered at the epicenter of each EQ, indicate the "critical zone" of each EQ as results from the corresponding calculated critical radius (km). Finally, the tectonic boundaries are shown with red solid curves [Bird, 2003].

5.2 Criticality Analysis by Wavelet Analysis

A very important source of information about the dynamics of a system recorded in the time domain, in the form of a time series, is the distribution of the waiting times of the time series. In case this distribution is expressed mathematically as an exponential distribution with a negative exponent, then this signifies the cutting off of the large correlation scales of the parts comprising the system, which is equivalent to a complete absence of dynamics [Contoyiannis et al., 2004, 2005]. Such a case is the generator of random numbers. At the opposite end of the dynamics spectrum is the power-law distribution where all the scales are present. Such a case is the critical state for every system [Schuster, 2005; Contoyiannis et al., 2002]. Most natural systems, and not only these, are organized in the time domain by means of the dynamics of intermittency. The term "intermittency" denotes an alternation, in which regions of low fluctuations (phase of "laminar regions") are interrupted by regions of intense outbreaks (phase of "bursts"). Due to the presence of the laminar regions, the intermittency presents stationarity characteristics. A "laminar region" is defined as the zone of the time series amplitude values between a specific, low enough, value of time series, the "start of the laminar region", and a higher value that delimits the transition to the phase of the bursts, the "end of the laminar region". The waiting times for which the time series values continuously remain within this zone are known as "laminar lengths". Therefore, finding the distribution of waiting times is related to finding the distribution of laminar lengths, as previously defined.

The most fundamental element for the calculation of the laminar lengths is the so-called "fixed point", which serves as the start of the laminar region and remains constant during laminar lengths' calculations. This is determined as the time series value for which the peak of the distribution of the time series values appears. In practice, this corresponds to the point, around the peak of the values' distribution, at which the steepest end of the distribution is observed. On the other hand, the end of the laminar region is treated as a free parameter and is located on the smooth side of the peak of the distribution of the time series values. Thus, the range of time series values around the peak of the values' distribution which is delineated between these two points is defined as the laminar region.

As already mentioned, the end of the laminar region is treated as a free parameter, so, by changing its position, it is possible that for a range of ends of the laminar region the corresponding laminar lengths' distributions can closely approach a power-law distribution, if of course such a power-law behavior is really embedded in the time series under analysis.

Given the table of values of the laminar lengths, one can find the laminar lengths' distribution as well as the corresponding exponent if it turns out to be a power-law. According to the method of critical fluctuations (MCF), if the exponent of the power-law lies in the range [1,2), then the system which creates the time series is in critical state [Potirakis et al., 2018; 2019b; 2021]. To calculate the laminar lengths' distribution as well as the exponent, if there is a power-law, in the following analysis examples we use a method that has recently been introduced, specifically, the wavelet-based detection of scaling behavior in noisy experimental data [Contoyiannis et al., 2020]. As it is explained in the following, this method has significant advantages in detecting scaling behavior over standard curve fitting-based methods.

Any function can be expanded on a wavelet basis, while wavelet expansion is suitable for phenomena that exhibit self-similarity, such as critical phenomena, manifested by power-law behavior. In discrete form, the mother wavelet function, $\psi(x)$, undergoes two transformations, the change of the scale j and the displacement k, with $j,k \in \mathbb{Z}$, producing the wavelet basis elements: $\psi_{j,k}(x) = 2^{\frac{j}{2}}\psi\left(2^j x - k\right)$, with $j = \cdots, -1,0,1, \ldots$ and $k = -j, \ldots, -1,0,1, \ldots, j$, whereas the wavelet analysis coefficients are denoted $d_{j,k}$. For $j = k = 0$ one gets the coarse-graining description of the analysis. In the framework of this description, the coefficients of the analysis can and do ignore the noise of the signal to be analyzed [Contoyiannis et al., 2020]. This behavior has been used to develop an algorithm that applies to any discrete distribution, $P(i), i = 1,2, \ldots, N_P$, associated with real or numerical time series. This algorithm can and does answer the question of whether the analyzed distribution embeds a power-law behavior, how close or far is it from the power-law, and calculates the corresponding power-law exponent p. In other words, it provides a kind of "fitting" result that can be applied to laminar lengths' distribution, without carrying the pathogeny of standard curve fitting-based methods due to noise in the experimental data, especially at the high values of the laminar lengths. In standard curve fitting, for a fitting function to avoid the tail of distributions where the strong noise makes the results vague, one usually keeps only the short scales for an analysis of the laminar lengths' distribution. But this is not correct because it brutally removes any information that the long scales may carry. In most cases of calculating the power-law from distributions of waiting times L presented in the literature, this is done on long scales ($L \gg 1$). Thus, long scales carry important information and cannot be excluded from the analysis. The wavelet basis used to

develop the specific algorithm is the Haar wavelet. The mother function of the Haar wavelets is defined, using the Heaviside step function, $\Theta(z)$, as:

$$\psi_H(x) = \Theta\left(\frac{\Delta}{2} - x\right)\Theta(x) - \Theta\left(x - \frac{\Delta}{2}\right)\Theta(\Delta - x), \tag{4}$$

for $x \in (0, \Delta]$, while the wavelet analysis coefficients for the expansion of a power-law function (appropriate for a finite system) $F(x) = \begin{cases} 0, & x \notin [\Delta_{min}, \Delta_{max}) \\ cx^{-p}, & \Delta_{min} \leq x < \Delta_{max} \end{cases}$ can be written as [Contoyiannis et al., 2020]:

$$d_{j,k} = c\sqrt{\frac{2^j}{\Delta}}\left(\sum_{i=max\left(\left[k\frac{\Delta}{2^j}\right],1\right)}^{\left[k\frac{\Delta}{2^j}+\frac{\Delta}{2^{j+1}}\right]} i^{-p} - \sum_{i=\left[k\frac{\Delta}{2^j}+\frac{\Delta}{2^{j+1}}\right]+1}^{\left[(k+1)\frac{\Delta}{2^j}\right]} i^{-p}\right), \tag{5}$$

where c is a normalization constant and $[z]$ stands for the integer part of a variable z.

One can then define the following quantities [Contoyiannis et al., 2020] for the discrete case:

$$\lambda = \frac{\frac{d_{00}}{d_{10}}}{\frac{d_{10}}{d_{20}}} = \frac{d_{00}d_{20}}{d_{10}^2} = \frac{\left(\sum_{i=1}^{\left[\frac{\Delta}{2}\right]} P(i) - \sum_{\frac{\Delta}{2}}^{\Delta} P(i)\right)\left(\sum_{i=1}^{\left[\frac{\Delta}{8}\right]} P(i) - \sum_{\left[\frac{\Delta}{8}\right]}^{\left[\frac{\Delta}{4}\right]} P(i)\right)}{\left(\sum_{i=1}^{\left[\frac{\Delta}{4}\right]} P(i) - \sum_{\left[\frac{\Delta}{4}\right]}^{\left[\frac{\Delta}{2}\right]} P(i)\right)^2} \tag{6}$$

and

$$R = \frac{d_{00}}{d_{10}} = \frac{1}{\sqrt{2}}\frac{\left(\sum_{i=1}^{\left[\frac{\Delta}{2}\right]} P(i) - \sum_{\frac{\Delta}{2}}^{\Delta} P(i)\right)}{\left(\sum_{i=1}^{\left[\frac{\Delta}{4}\right]} P(i) - \sum_{\left[\frac{\Delta}{4}\right]}^{\left[\frac{\Delta}{2}\right]} P(i)\right)}, \tag{7}$$

with $8 < \Delta < N_P$.

The proposed method for revealing the criticality and finding the exponent of the power-law of the distribution of laminar lengths comprises the following steps:

1) We apply Eq. (6) to calculate λ as a function of Δ up to a value $\Delta_{max} \leq N_P$. We plot λ vs Δ, and since we are interested in the convergence of λ [Contoyiannis et al., 2020], we focus on the right-most part of the plot (for large Δ), while up to the last 10 points, i.e., $n = \Delta_{max} - 9, \ldots, \Delta_{max}$ (see also Eq. (8)) are enough to deduce a conclusion. The value of Δ_{max} is determined in the tail of the distribution of laminar lengths according to the next criterion.
2) We quantify the previous step by calculating the distance of λ from the value $\lambda = 1$, which denotes a perfect power-law, by calculating the quantity:

$$Q_\lambda = \frac{1}{10}\sum_{n=\Delta_{max}-9}^{\Delta_{max}} (1 - \lambda_n)^2. \tag{8}$$

The closer the Q_λ is to the value 0 the closer to the power-law is the distribution. So, the position of Δ_{max} is located where the quantity Q_λ comes closest to zero.

3) Then, we produce the R vs Δ plot, using Eq. (7). From the convergence region of the plot, i.e., for $n = \Delta_{max} - 9, \ldots, \Delta_{max}$ (see Eq. (8)), a mean value, $\langle R \rangle$, is obtained for the quantity R.
4) We consider the test function $f(i) = c_f i^{-p}$, $i = 1,2,..\Delta_{max}$, where c_f is a constant factor, and by putting $f(i)$ in place of $P(i)$, we solve Eq. (7) numerically for the given $\langle R \rangle$ value with respect to p, to estimate the value of p exponent which corresponds to $\langle R \rangle$.

The power-law test function mentioned in Step 4 is used only when $Q_\lambda < order(10^{-3})$, which indicates an exact power-law, and further if $p \in [1,2)$ this indicates that the underlying system is in critical state. In case that $order(10^{-3}) < Q_\lambda < order(10^{-2})$, this indicates that the examined laminar lengths' distribution is close to power-law. In this case, in Step 4 we can use a truncated power-law test function $g(i) = c_g i^{-p_2} e^{-ip_3}, i = 1,2,..\Delta_{max}$ where c_g is a constant factor, instead of a power-law test function $f(i)$, to further investigate. So, we quantify a power-law with an exponential correction, and if the exponents are found to be $p_2 \in [1,2)$ and $p_3 \approx 0$, this indicates that the underlying system is in critical state. In cases that Q_λ turns out to be higher than the $order(10^{-3})$ there is no power-law distribution.

5.3 Analysis Results

The purpose of the wavelet-based analysis presented in Section 5.2 is to investigate: (a) if a time window of the MHz recordings (a MHz time series excerpt) of a station close to the epicenter of an EQ indicates that the underlying EQ preparation system is in critical state, or how close or how far from it is, and (b) in case that it is in critical state, to calculate the exact exponent of the power-law that describes the distribution of laminar lengths (waiting times). The calculation is considered accurate because it takes into account all the scales of the laminar lengths' distribution, especially it provides accurate calculations for large scales, in which the results of standard curve fitting-based methods are unreliable: (a) due to the small statistics in the tail of the distribution, and (b) due to the large noise in the tail region. In the following we present a few examples of MHz signals' analysis possibly related to the recent significant EQs presented in Section 5.1.

5.3.1 2020 Samos EQ

Figure 24 shows the 41 MHz signal (of 172800 sec duration) recorded by the "M" station located in Agia Paraskevi, Lesvos Island (see Table 1 and Fig. 23), during a time period of two days from 27/10/2020 to 28/10/2020, 3-2 days before the 2020 Samos EQ (see Table 4 and Fig. 23). Here, the measured quantity, denoted by ϕ (a.u.), is the amplitude of the 41 MHz receiver's voltage output. Following the steps of the wavelet-based criticality analysis method presented in Section 5.2, it was found that the blue-colored excerpt of the specific MHz signal of Fig. 24 (of 90000 sec duration, i.e., ~3 days before the EQ) presents criticality characteristics. Figure 25a shows the amplitude's

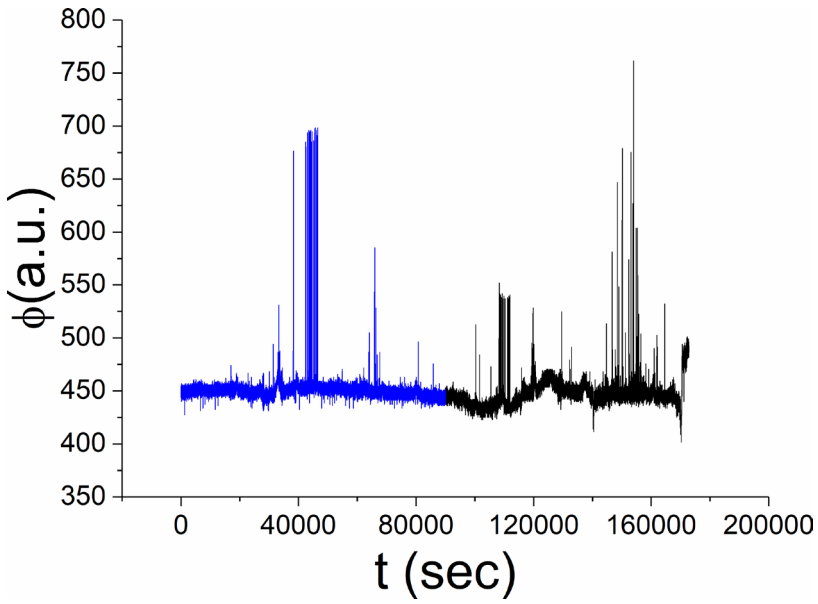

Figure 24. Temporal evolution of 41 MHz time series (27/10/2020-28/10/2020), recorded by station M before the occurrence of the 2020 Samos EQ (see Table 4 and Fig. 23). The blue-colored excerpt of the time series, according to the analysis performed, presents critical behavior (see text).

distribution of the analyzed blue-colored excerpt of Fig. 24. The laminar region for the construction of laminar lengths' distribution (see Fig. 25b) was found to be $\phi \in [440,456]$. In the next step, using the laminar lengths' distribution, we calculated the λ as a function of Δ using Eq. (6), the plot of which for the last 10 values of Δ (the last value is $\Delta_{max} = 115$) is shown in Fig. 26. From this, we found that $Q_\lambda = 1.6 \cdot 10^{-4}$ (see Eq. (8)), which is $<10^{-3}$, indicating an exact power-law laminar lengths' distribution (see Section 5.2). Moreover, in order to calculate the exponent p of the power-law, the quantity R was computed as a function of Δ (see Eq. (7)). In Fig. 27, the plot of R vs Δ is depicted for the last 10 values of Δ, used to estimate the mean value of R at the convergence region as $\langle R \rangle = 0.82$. Finally, by using the test function $f(i) = ci^{-p}, i = 1,2,..\Delta_{max}$ and solving Eq. (7) numerically for with respect to p, it was found that $p = 1.12$ (i.e., $p \in [1,2)$), confirming the existence of criticality.

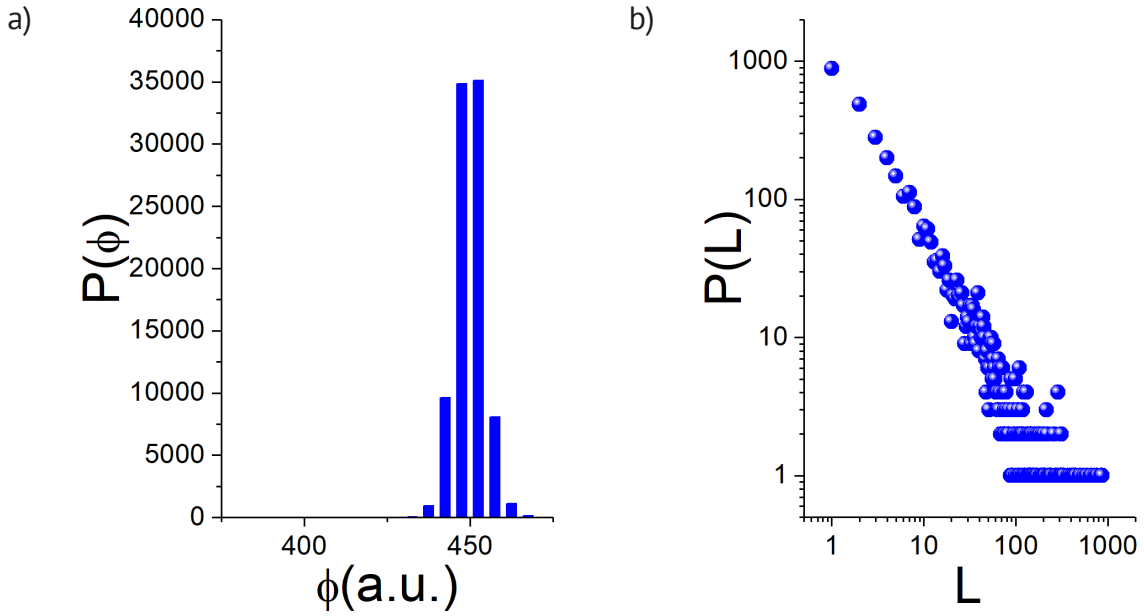

Figure 25. (a) Amplitude values' distribution of the blue-colored excerpt of the time series presented in Fig. 24. (b) The distribution of laminar lengths of the corresponding excerpt, considering the laminar region $\phi \in [440,456]$.

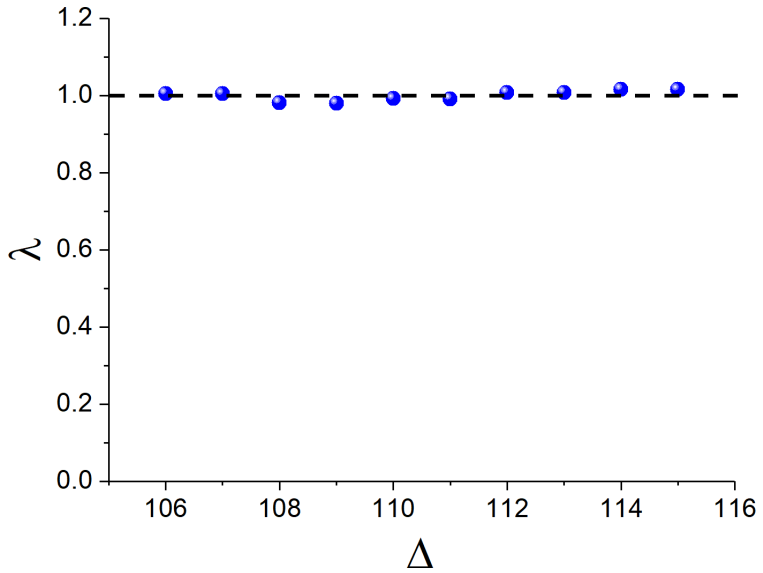

Figure 26. Plot of λ vs Δ (blue dots) for the last 10 values of Δ, as computed (see Eq. (6)) for the distribution of laminar lengths shown in Fig. 25b. The horizontal black dashed line corresponds to the criterion $\lambda = 1$, which denotes a perfect power law distribution.

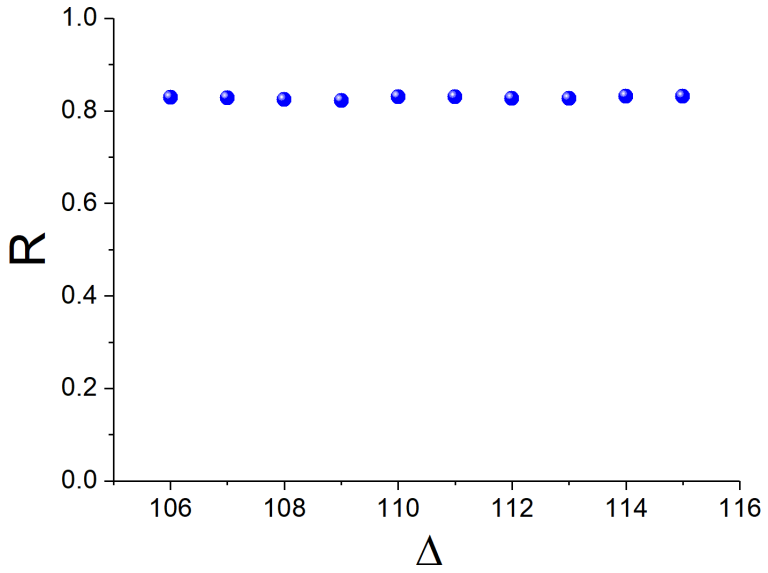

Figure 27. Plot of R vs Δ (blue dots) for the last 10 values of Δ, as computed (see Eq. (7)) for the distribution of laminar lengths shown in Fig. 25b. The mean value of these 10 values is $\langle R \rangle = 0.82$.

5.3.2 2020 Crete EQ

Another example of ELSEM-Net time series excerpt for which criticality was detected is the case of the 2020 Crete EQ (see Table 4 and Fig. 23). More specifically, in Fig. 28 a 41 MHz time series excerpt, spanning the dates 28/04/2020-02/05/2020 is shown, recorded 4-0 days prior to the occurrence of the EQ by the "V" station located in Vamos, Crete Island (see Table 1 and Fig. 23). The blue-colored part of the specific signal, with a duration of 185000 sec, i.e., 4-2 days before the EQ, was found to present criticality characteristics.

Figure 29a depicts the amplitude's distribution of the analyzed (blue-colored) excerpt of Fig. 28. The laminar region for the construction of laminar lengths' distribution (see Fig. 29b) was found to be $\phi \in [210,240]$. Figure 30

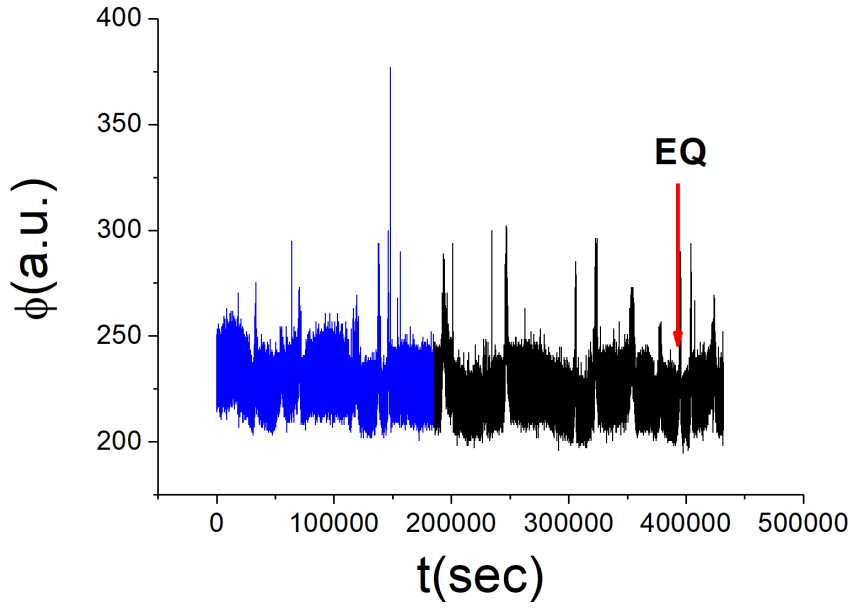

Figure 28. Temporal evolution of the 41 MHz time series (28/04/2020-02/05/2020), recorded by station V before, during and after the occurrence of 2020 Crete EQ (see Table 4 and Fig. 23). The blue-colored excerpt of the time series, according to the analysis performed, presents critical behavior (see text). The red arrow marks the time of the occurrence of the EQ.

portrays the last 10 values of λ as a function of Δ ($\Delta_{max} = 264$), calculated for laminar lengths' distribution of 29b using Eq. (6), which indicates that laminar lengths' distribution is very close to a power-law distribution. Specifically, using Eq. (8), we found that $Q_\lambda = 1.35 \cdot 10^{-3}$. According to Section 5.2, this means that the value of Q_λ is of order of 10^{-3}, and therefore the laminar lengths' distribution is very close to (but not exactly) power-law, therefore we used a truncated power-law test function $g(i) = ci^{-p_2}e^{-ip_3}, i = 1,2,..\Delta_{max}$ instead of a power-law test function to numerically solve Eq. (7). In order to determine the exponents p_2 and p_3, we need first to determine $\langle R \rangle$. In Fig. 31 the plot of R vs Δ is provided for the last 10 values of Δ, used to estimate the mean value of R at the convergence region as $\langle R \rangle = 0.7468$. Finally, by using the test function $g(i)$ and solving Eq. (7) numerically for $\langle R \rangle = 0.7468$ with respect to p_2 and p_3, it was found that $p_2 = 1.30$ (i.e., $p_2 \in [1,2)$) and $p_3 = 0.009$ (i.e., $p_3 \approx 0$), confirming the existence of criticality.

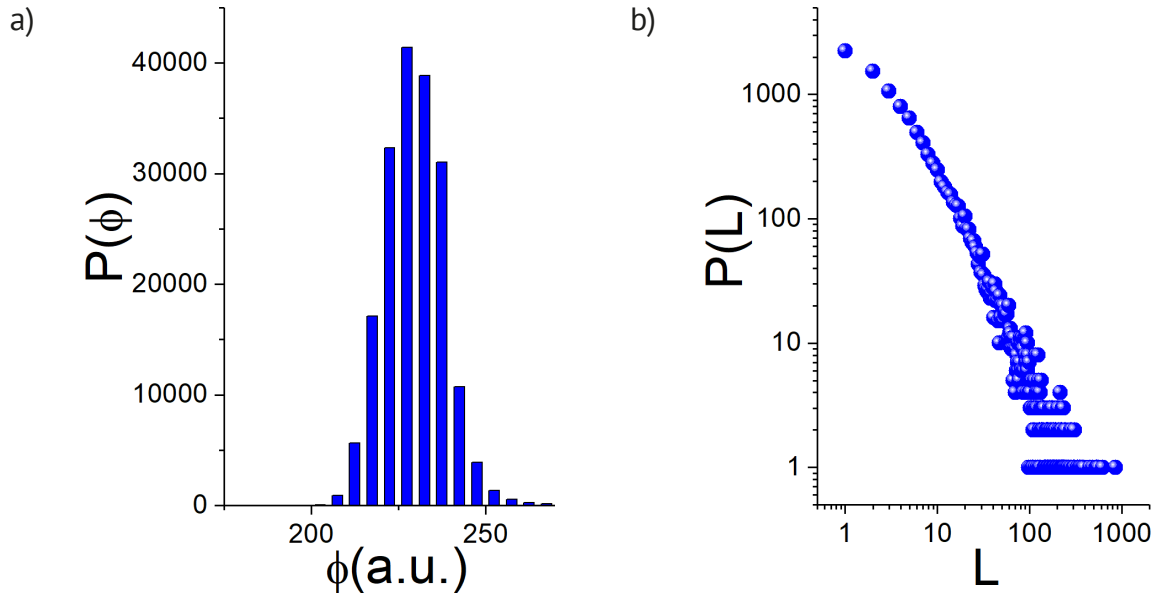

Figure 29. (a) Amplitude values' distribution of the blue-colored excerpt of the time series presented in Fig. 28. (b) The distribution of laminar lengths of the corresponding excerpt, considering the laminar region $\phi \in [210,240]$.

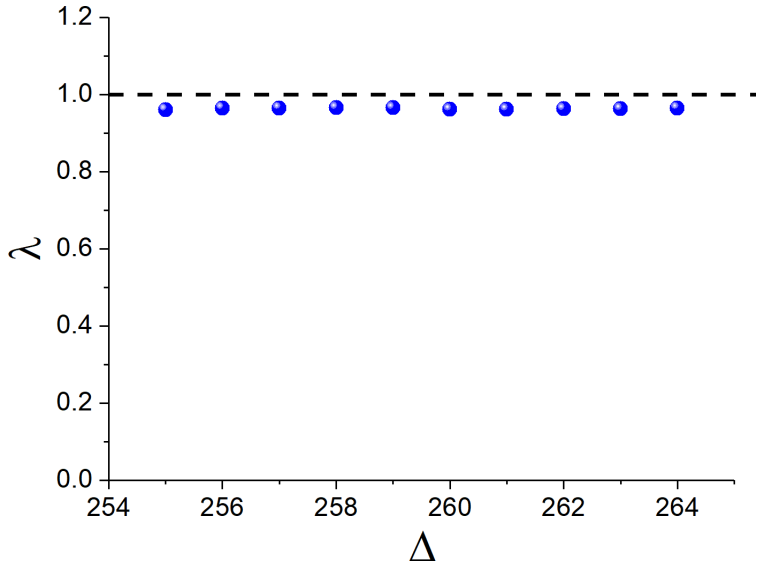

Figure 30. Same as Fig. 26 for the distribution of laminar lengths shown in Fig. 29b.

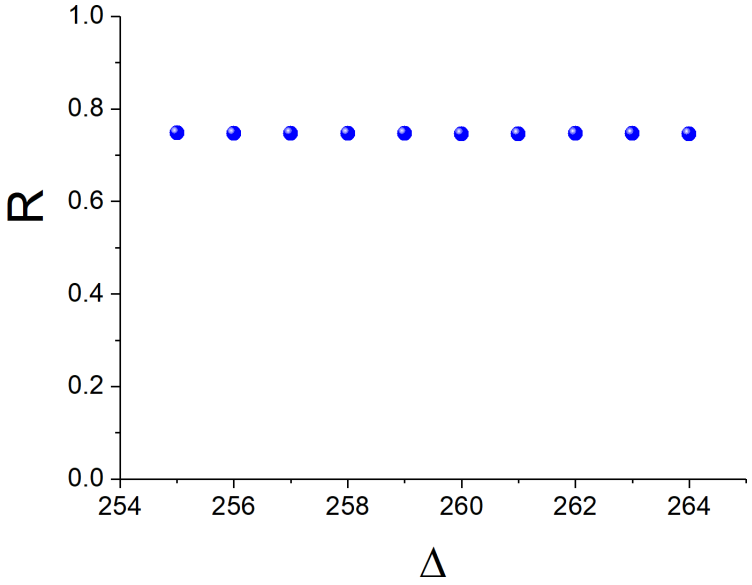

Figure 31. Same as Fig. 27 for the distribution of laminar lengths shown in Fig. 29b. The mean value of these 10 values is $\langle R \rangle = 0.7468$.

5.3.3 2023 Rhodes EQ

The last analysis example concerns an EQ which occurred east-southeast to Rhodes Island in Greece on January 2023 (see Table 4 and Fig. 23). In Fig. 32 we present the temporal evolution of the 41 MHz signal recorded 3-0 days (22/01/2023-25/01/2023) before the specific EQ, as received by the ELSEM-Net station with station code "A" located in Archangelos, Rhodes Island (see Table 1 and Fig. 23). The different colors of excerpts of the time series, as shown in Fig. 32, correspond to the different dynamics. As proved by the analysis results presented in the following, the blue-colored excerpt was found to present criticality 3-2 days before the occurrence of the EQ. However, in the red- and green-colored excerpts critical dynamics are absent. On the other hand, as indicated by its amplitudes' distribution (not shown here), in the black-colored excerpt a "phase transition" is embedded, which is characterized as the "symmetry-breaking phenomenon", explained in detail in Contoyiannis et al. [2018]. In such time series, as the specific black-colored excerpt, the wavelet-based criticality analysis method employed here (see Section 5.2) is not possible to be applied due to the lack of stationarity of the time series, so such time series are analyzed as in Contoyiannis et al. [2018]. Finally, the last excerpt of Fig. 32 (violet-colored), which was recorded after the EQ occurrence, also doesn't present any indication of criticality, implying that another strong EQ was not expected to occur close after the 2023 Rhodes EQ, as indeed happened. It has to be mentioned here that similar behavior, i.e., departure from critical state before the EQ occurrence and no critical dynamics after the EQ occurrence, was found (not presented here) for the MHz recordings related to the cases of the 2020 Samos EQ and the 2020 Crete EQ. It is noted that the specific behavior is fully compatible with the four-stage model for EQ generation (FSMEG) presented in Section 1.

Figure 33 portrays the amplitudes' distributions of the colored excerpts of Fig. 32 (except for that of the black-colored for the above-mentioned reason). In Fig. 34 the corresponding laminar lengths' distributions of the colored excerpts of Fig. 32 are shown. The chosen laminar regions of each laminar lengths' distribution (Figs. 34a-34d) were found to be $\phi \in [410{,}460]$, $\phi \in [430\text{–}458]$, $\phi \in [405\text{–}428]$ and $\phi \in [400\text{–}422]$, respectively. In Figs. 35a-35d, the λ vs Δ (see Eq. (6)) plots are shown for the corresponding laminar lengths' distributions of Figs. 34a-34d, as calculated for the last 10 values of Δ, while the Δ_{max} values were 218, 201, 170 and 123, respectively. By using the Eq. (8), the corresponding Q_λ values for the above-mentioned Δ_{max} values were found to be $7 \cdot 10^{-4}$, $1.45 \cdot 10^{-2}$, $5 \cdot 10^{-2}$ and $6 \cdot 10^{-2}$, respectively. Thus, only the blue-colored excerpt of Fig. 32, resulted to a Q_λ value lower than $order(10^{-3})$ ($Q_\lambda = 7 \cdot 10^{-4} < 10^{-3}$). So, according to Section 5.2, only the specific excerpt of 41 MHz recordings presents criticality, with an exact power law laminar lengths' distribution. For the specific time series excerpt, using Eq. (7), the quantity R was calculated for the last 10 values of Δ, from which it was found that $\langle R \rangle = 0.7283$. Finally, using the test function $f(i) = ci^{-p}, i = 1{,}2{,}..\Delta_{max}$ and solving Eq. (7) numerically for $\langle R \rangle = 0.7283$ with respect to p, it was found that $p = 1.64$ (i.e., $p \in [1{,}2)$), confirming the existence of criticality.

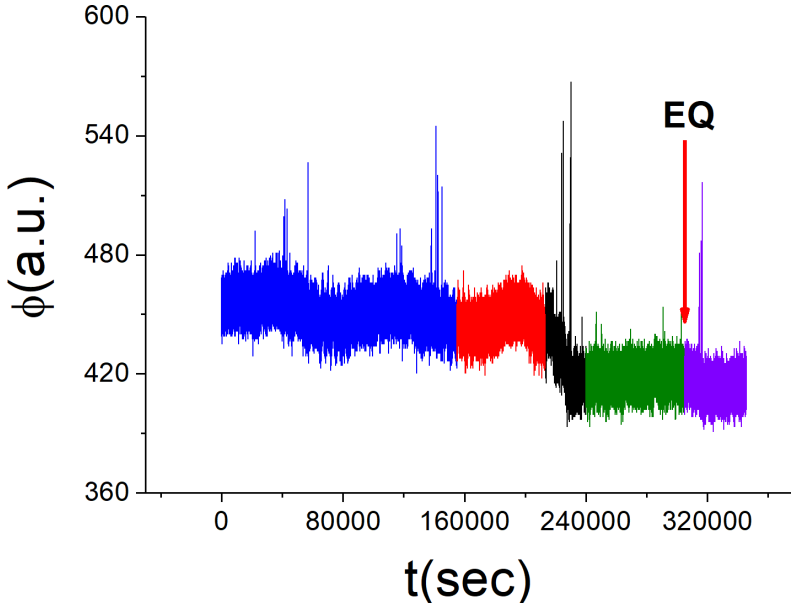

Figure 32. Temporal evolution of the 41 MHz time series (22/01/2023-25/01/2023), recorded by station A before, during and after the occurrence of 2023 Rhodes EQ (see Table 4 and Fig. 23). The blue-colored excerpt of the time series, according to the analysis performed, presents critical behavior (see text). The red- and green-colored excerpts don't present critical dynamics, while the black-colored excerpt is a "symmetry-breaking window" (see text). The violet-colored excerpt, recorded after the occurrence of the EQ, also doesn't present critical dynamics. The red arrow marks the time of the occurrence of the EQ.

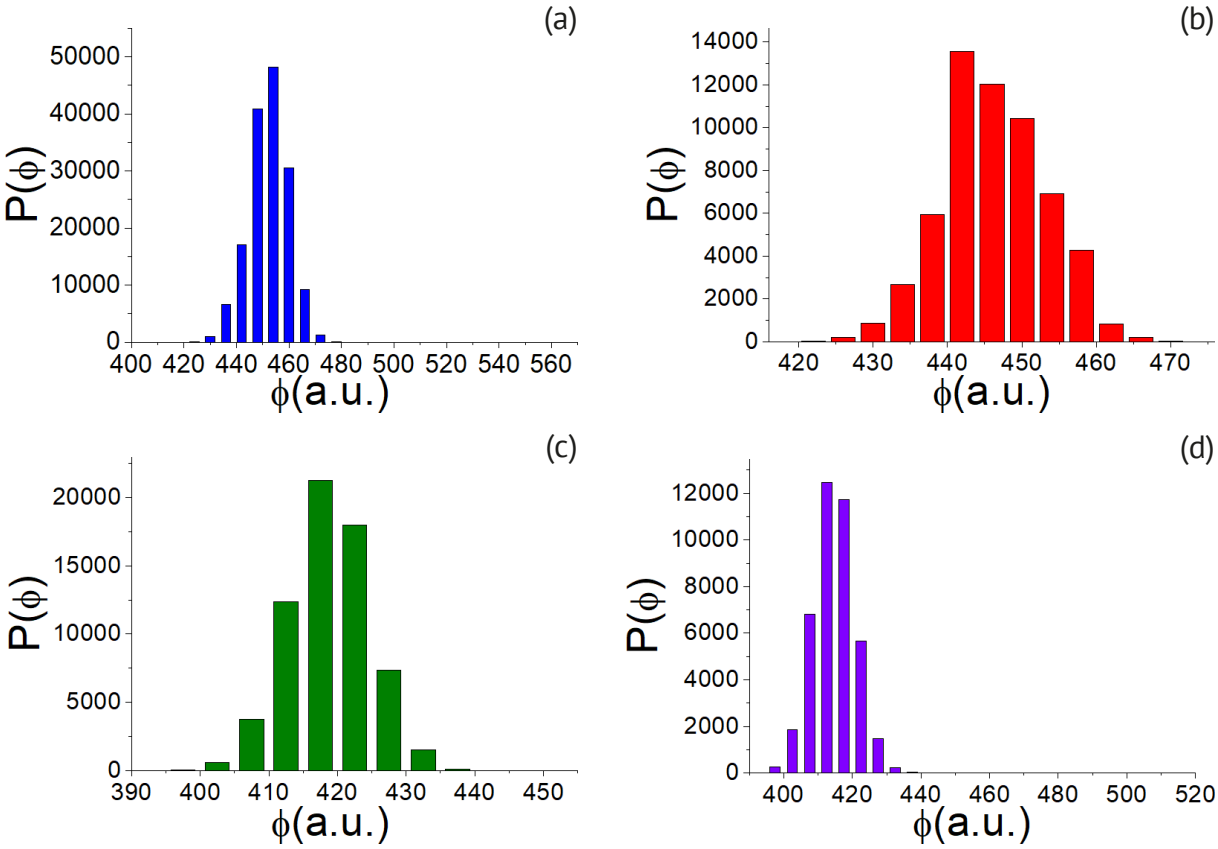

Figure 33. Amplitudes' distributions of the correspondingly-colored excerpts shown in Fig. 32 (the amplitude distribution of the black-colored excerpt is not presented).

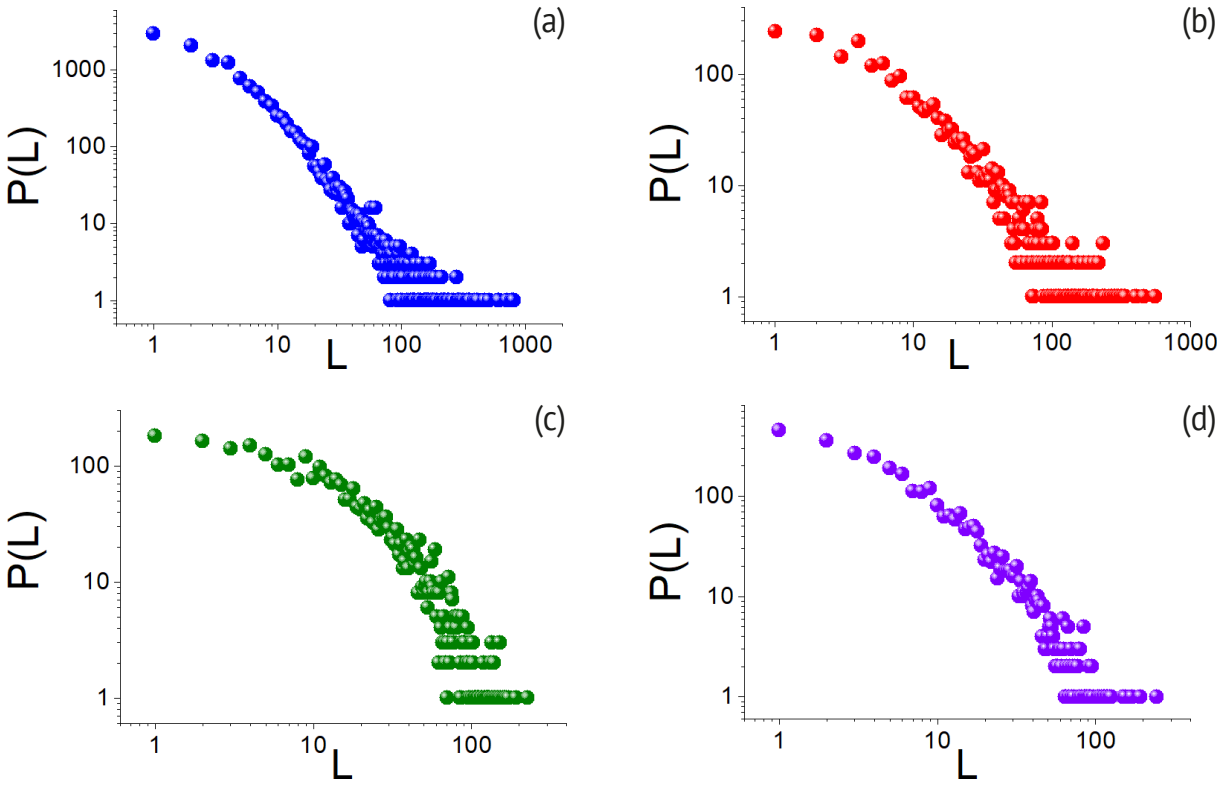

Figure 34. Laminar lengths' distributions of the correspondingly-colored excerpts shown in Fig. 32. The considered laminar regions for each laminar lengths' distribution are: (a) 410-460, (b) 430-458, (c) 405-428, (d) 400-422.

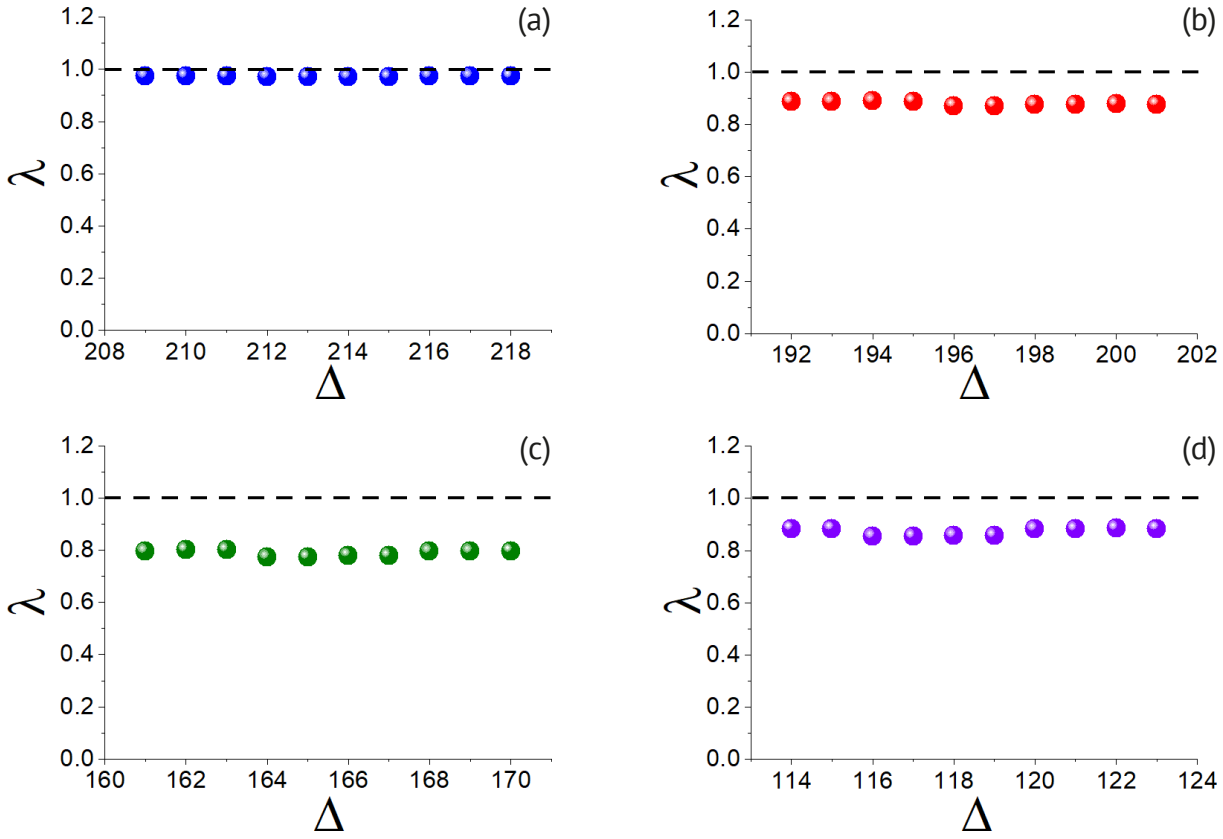

Figure 35. Same as Fig. 26 for the distributions of laminar lengths shown in: (a) Fig. 34a, (b) Fig. 34b, (c) Fig. 34c, (d) Fig. 34d. Only Fig. 35a indicates a power-law laminar lengths' distribution.

6. Conclusion

In this paper, we presented, for the first time in detail, the structure, instrumentation, and management of the hELlenic Seismo-ElectroMagnetics Network (ELSEM-Net, http://elsem-net.uniwa.gr), a network of telemetric stations covering Greece and operating for > 20 years for the detection of MHz-kHz FEME/FEMR prior to strong EQs with epicenters on land or near the coast-line. Given the fact that the used instrumentation is not commercially available, but has been specifically designed and implemented by the research team of ELSEM-Net for the purposes of that particular network, we hope that the provided detailed presentation would be a valuable contribution to any interested research teams around the world (focusing either to natural or man-induced EQs, i.e., to global fractures at the large and intermediate scale) to install and operate their own networks. Such a perspective would be very important for the in-depth research of this kind of observables and the associated processes, as it will allow the accumulation of directly compatible data, possibly associated with different kinds of EQs from different parts of the world. Yet another, important contribution of the provided information is that allows for the integration of MHz-kHz FEME/FEMR to the future development of multi-observables-based EQ forecasting systems, which will combine information from a wide range of ground-based and space-born direct or indirect EQ-related observables. It should also be mentioned that we intend to further develop ELSEM-Net's website (http://elsem-net.uniwa.gr) (last accessed on 14 May 2023), so that any scientist can have free access to updated information related to the instrumentation used by ELSEM-Net, since we intend to continue the instrumentation development.

Finally, in this article, we presented for the first time the application of a very recently introduced time series analysis method, which relies on wavelet analysis to achieve a coarse-graining that permits the accurate extraction of dynamics information from noisy data, to MHz FEME/FEMR. From the results obtained for three cases of recent significant EQs ($M_W \geq 5.9$) that occurred in 2020 and 2023 in Greece, it is concluded that criticality was reached a few days (4-2 days, depending on the case) prior to each EQ. Specifically for the last presented case of the 2023 Rhodes EQ, we also showed that the MHz recordings following the MHz time series excerpt which was found to follow criticality dynamics, don't present critical dynamics, either these precede or follow the occurrence of the specific EQ, which is fully compatible with the four-stage model for EQ generation (FSMEG) presented in Section 1.

Acknowledgements. The authors would like to express their gratitude to University of West Attica that financially supports the maintenance and expansion of ELSEMNet. The authors would like to thank Dr. D. Doukakis for suggesting us use the "Waveshare Raspberry Pi High-Precision AD/DA Expansion Board" for the new ELSEM-Net Raspberry Pi-based datalogger, as well as Dr. J. Kopanas and Dr. G. Antonopoulos for their fieldwork at the Zakynthos station, and all other members of ELSEM-Net for their valuable support in operating ELSEM-Net. Finally, the ELSEM-Net team would like to express respect and gratitude to the late founder of ELSEM-Net Prof. Constantinos Nomicos for his vision, dedication, guidance and constant support which made the research on geophysical scale fracture-induced MHz-kHz electromagnetic emissions possible.

References

Baddari, K. and A.D. Frolov (2011). Regularities in discrete hierarchy seismo-acoustic mode in a geophysical field, Ann. Geophys., 53, 5-6, https://doi.org/10.4401/ag-4725

Balanis, C. (2005). Antenna Theory: Analysis and Design, John Willey and Sons, Hoboken.

Bird, P. (2003). An updated digital model of plate boundaries, Geochemistry, Geophys. Geosystems, 4, 3, 1-52, https://doi.org/10.1029/2001gc000252

Bowman, D.D., G. Ouillon, C.G. Sammis, A. Sornette and D. Sornette (1998). An observational test of the critical earthquake concept, J. Geophys. Res. Solid Earth, 103, 24359-24372, https://doi.org/10.1029/98jb00792

Brener, E.A. and E. Bouchbinder (2021). Unconventional singularities and Energy Balance in frictional rupture, Nat. Commun., 12, 1, 1-9, https://doi.org/10.1038/s41467-021-22806-9

Carpinteri, A., G. Lacidogna, A. Manuello, G. Niccolini, A. Schiavi and A. Agosto (2011). Mechanical and electromagnetic emissions related to stress-induced cracks, Exp. Tech., 36, 3, 53-64, https://doi.org/10.1111/j.1747-1567.2011.00709.x

Carpinteri, A. and O. Borla (2017). Fracto-emissions as seismic precursors, Eng. Fract. Mech., 177, 239-250, https://doi.org/10.1016/j.engfracmech.2017.03.007

Carr, J.J. and G.W. Hippisle (2012). Practical Antenna Handbook, McGraw-Hill, New York.

Chelidze, T., F. Vallianatos and L. Telesca (2018). Complexity of seismic time series: Measurement and Application, Elsevier, Amsterdam, https://doi.org/10.1016/C2016-0-04546-1

Contoyiannis, Y. and S.M. Potirakis (2018). Signatures of the symmetry breaking phenomenon in pre-seismic electromagnetic emissions, J. Stat. Mech., 2018, 8, 083208, https://doi.org/10.1088/1742-5468/aad6ba

Contoyiannis, Y.F., F.K. Diakonos and A. Malakis (2002). Intermittent dynamics of critical fluctuations, Phys. Rev. Lett., 89, 035701, https://doi.org/10.1103/PhysRevLett.89.035701

Contoyiannis, Y.F., F.K. Diakonos, C. Papaefthimiou and G. Theophilidis (2004). Criticality in the relaxation phase of a spontaneously contracting atria isolated from a frog's heart, Phys. Rev. Lett., 93, 098101, https://doi.org/0.1103/PhysRevLett.93.098101

Contoyiannis, Y.F., P.G. Kapiris, and K.A. Eftaxias (2005). Monitoring of a preseismic phase from its electromagnetic precursors, Phys. Rev. E, 71, 6, https://doi.org/10.1103/physreve.71.066123

Contoyiannis, Y.F., S.M. Potirakis and K. Eftaxias (2013). The Earth as a living planet: human-type diseases in the earthquake preparation process, Nat. Hazards Earth Syst. Sci., 13, 125-139, http://dx.doi.org/10.5194/nhess-13-125-2013.

Contoyiannis, Y., S.M. Potirakis, K. Eftaxias and L. Contoyianni (2015). Tricritical crossover in earthquake preparation by analyzing preseismic electromagnetic emissions, J. Geodyn., 84, 40-54, https://doi.org/10.1016/j.jog.2014.09.015

Contoyiannis, Y.F., S.M. Potirakis and F.K. Diakonos (2020). Wavelet-based detection of scaling behavior in noisy experimental data, Phys. Rev. E, 101, 052104, https://doi.org/10.1103/PhysRevE.101.052104

Daniliev, S., N. Danilieva, S. Mulev and V. Frid (2022). Integration of seismic refraction and fracture-induced electromagnetic radiation methods to assess the stability of the roof in mine-workings, Minerals, 12, 5, 609, https://doi.org/10.3390/min12050609

Das, S., J. Mallik, S. Dhankhar, N. Suthar, A.K. Singh, V. Dutta, U. Gupta, G. Kumar and R. Singh (2020). Application of fracture induced electromagnetic radiation (FEMR) technique to detect landslide-prone slip planes, Nat. Hazards, 101, 2, 505-535, https://doi.org/10.1007/s11069-020-03883-3

Department of National Defense and Department of Transport and Communications (Greece) (2006). National Regulation of Allocation of Frequency Bands. Government Gazette of the Hellenic Republic, Part 2, 399 (3 April 2006), 4877-4962 (in Greek), Online available: http://www.eett.gr/opencms/export/sites/default/EETT_EN/Electronic_Communications/Radio_Communications/TelecommunicationEquipment/FEK399.pdf (last accessed on 14 May 2023)

Dolu, A. and H. İkizler (2022). The effects of major earthquakes on the labor market: Evidence from Turkey, Int. J. Soc. Econ., 50, 5, 662-674, https://doi.org/10.1108/ijse-08-2022-0568

Donner, R.V., S.M. Potirakis, G. Balasis, K. Eftaxias and J. Kurths (2015). Temporal correlation patterns in pre-seismic electromagnetic emissions reveal distinct complexity profiles prior to major earthquakes, Phys. Chem. Earth, 85-86, 44-55, https://doi.org/10.1016/j.pce.2015.03.008

Eftaxias, K. and S.M. Potirakis (2013). Current challenges for pre-earthquake electromagnetic emissions: Shedding light from micro-scale plastic flow, granular packings, phase transitions and self-affinity notion of fracture process, Non. Proc. in Geophys., 20, 5, 771-792, https://doi.org/10.5194/npg-20-771-2013

Eftaxias, K., P. Kapiris, J. Polygiannakis, N. Bogris, J. Kopanas, G. Antonopoulos, A. Peratzakis and V. Hadjicontis (2001). Signatures of pending earthquake from electromagnetic anomalies, Geophys. Res. Lett., 28, 17, 3321-3324, https://doi.org/10.1029/2001gl013124

Eftaxias, K., P. Kapiris, E. Dologlou, J. Kopanas, N. Bogris, G. Antonopoulos, A. Peratzakis and V. Hadjicontis (2002). EM anomalies before the Kozani earthquake: A study of their behavior through laboratory experiments, Geophys. Res. Lett., 29, 8, https://doi.org/10.1029/2001gl013786

Eftaxias, K., P. Frangos, P. Kapiris, J. Polygiannakis, J. Kopanas, A. Peratzakis, P. Skountzos and D. Jaggard (2004). Review and a model of pre-seismic electromagnetic emissions in terms of fractal electrodynamics, Fractals, 12, 02, 243-273. https://doi.org/10.1142/s0218348x04002501

Eftaxias, K., Y. Contoyiannis, G. Balasis, K. Karamanos, J. Kopanas, G. Antonopoulos, G. Koulouras and C. Nomicos (2008). Evidence of fractional-brownian-motion-type asperity model for earthquake generation in candidate pre-seismic electromagnetic emissions, Nat. Hazards Earth Syst. Sci., 8, 4, 657-669, https://doi.org/10.5194/nhess-8-657-2008

Eftaxias, K., S.M. Potirakis and T. Chelidze (2013). On the puzzling feature of the silence of precursory electromagnetic emissions, Nat. Hazards Earth Syst. Sci., 13, 2381-2397, https://doi.org/10.5194/nhess-13-2381-2013

Eftaxias, K., S.M. Potirakis and Y. Contoyiannis (2018). Four-Stage Model of Earthquake Generation in Terms of Fracture-Induced Electromagnetic Emissions Tamaz Chelidze, Filippos Vallianatos and Luciano Telesca (Editors), Complexity of Seismic Time Series Measurement and Application, 437-502, https://doi.org/10.1016/b978-0-12-813138-1.00013-4

Elliott, J.R., M. de Michele and H.K. Gupta (2020). Earth observation for crustal tectonics and earthquake hazards, Surv. Geophys., 41, 6, 1355-1389, https://doi.org/10.1007/s10712-020-09608-2

Enomoto, Y. and H. Hashimoto (1990). Emission of charged particles from indentation fracture of rocks, Nature, 346(6285), 641-643. https://doi.org/10.1038/346641a0

Fraser-Smith, A.C., A. Bernardi, P.R. McGill, M.E. Ladd, R.A. Helliwell and O.G. Villard (1990). Low-frequency magnetic field measurements near the epicenter of the Ms7.1 Loma Prieta earthquake, Geophys. Res. Let., 17, 9, 1465-1468, https://doi.org/10.1029/gl017i009p01465

Frid, V. and K. Vozoff (2005). Electromagnetic radiation induced by mining rock failure, Int. J. Coal Geology, 64, 1-2, 57-65, https://doi.org/10.1016/j.coal.2005.03.005

Frid, V., A. Rabinovitch and D. Bahat (2006). Crack velocity measurement by induced electromagnetic radiation, Phys. Let. A, 356, 2, 160-163, https://doi.org/10.1016/j.physleta.2006.03.024

Frid, V., A. Rabinovitch and D. Bahat (2020a). Earthquake forecast based on its nucleation stages and the ensuing electromagnetic radiations, Phys. Let. A, 384(4), 126102. https://doi.org/10.1016/j.physleta.2019.126102

Frid, V., A. Rabinovitch and D. Bahat (2020b). Seismic moment estimation based on fracture induced electromagnetic radiation, Eng. Geo., 274, 105692, https://doi.org/10.1016/j.enggeo.2020.105692

Frid, V., E.Y. Wang, S.N. Mulev and D.X. Li (2021). The fracture induced electromagnetic radiation: Approach and protocol for the Stress State Assessment for Mining. *Geotechnical and Geological Engineering*, 39(4), 3285-3291. https://doi.org/10.1007/s10706-021-01682-6

Geller, R.J. (1997). Earthquake prediction: A critical review, Geophys. J. Int., 131, 3, 425-450.,https://doi.org/10.1111/j.1365-246x.1997.tb06588.x

Gershenzon, N.I., M.B. Gokhberg, A.V. Karakin, N.V. Petviashvili and A.L. Rykunov, (1989). Modelling the connection between earthquake preparation processes and crustal electromagnetic emission, Phys. Earth Planet Inter., 57, 1-2, 129-138, https://doi.org/10.1016/0031-9201(89)90222-7

Gokhberg, M.B., V.A. Morgounov, T. Yoshino and I. Tomizawa (1982). Experimental measurement of electromagnetic emissions possibly related to earthquakes in Japan, J. Geophys. Res., 87, B9, 7824, https://doi.org/10.1029/jb087ib09p07824

Greiling, R.O. and H. Obermeyer (2010). Natural electromagnetic radiation (EMR) and its application in structural geology and neotectonics, J. Geol. Soc. India, 75, 1, 278-288, https://doi.org/10.1007/s12594-010-0015-y

Guo, Q., S. Yong and X. Wang (2021). Statistical analysis of the relationship between AETA electromagnetic anomalies and local earthquakes, Entropy, 23, 4, 411, https://doi.org/10.3390/e23040411

Hadjicontis, V., C. Mavromatou, D. Mastrogiannis, T.N. Antsygina and K.A. Chishko (2011). Relationship between electromagnetic and acoustic emissions during plastic deformation of gamma-irradiated LIF monocrystals, J. App. Phys., 110, 2, 024907, https://doi.org/10.1063/1.3608247

Han, P., K. Hattori, M. Hirokawa, J. Zhuang, C.-H. Chen, F. Febriani, H. Yamaguchi, C. Yoshino, J.-Y. Liu and S. Yoshida (2014). Statistical analysis of ULF seismomagnetic phenomena at Kakioka, Japan, during 2001-2010, J. Geophys. Res. Space Physics, 119, 6, 4998-5011, https://doi.org/10.1002/2014ja019789

Hattori, K. (2013). ULF geomagnetic changes associated with major earthquakes, in Earthquake Prediction Studies, Seismo Elecromagnetics M. Hayakawa (Editor), Terra Scientific Publication Company, Tokyo, Japan,

Hayakawa, M. (2015). Earthquake prediction with Radio Techniques, John Wiley & Sons, Singapore, https://doi.org/10.1002/9781118770368

Hayakawa, M. (2019). Seismo electromagnetics and earthquake prediction: History and new directions, Int. J. earthquake Res., 06, 01, 1-23, https://www.researchgate.net/profile/Masashi-Hayakawa-2/publication/335877495_Seismo_Electromagnetics_and_Earthquake_Prediction_History_and_New_directions/links/5fa74db2458515157bf6dc3d/Seismo-Electromagnetics-and-Earthquake-Prediction-History-and-New-directions.pdf

Hayakawa, M. and O.A. Molchanov (2002). Seismo electromagnetics: Lithosphere-atmosphere-ionosphere coupling, Terra Scientific Publication Company, Tokyo.

Hayakawa, M., Y. Kasahara, T. Nakamura, F. Muto, T. Horie, S. Maekawa, Y. Hobara, A.A. Rozhnoi, M. Solovieva and O.A. Molchanov (2010). A statistical study on the correlation between lower ionospheric perturbations as seen by subionospheric VLF/LF propagation and earthquakes, J. Geophys. Res. Space Phys., 115, A9, 1-9, https://doi.org/10.1029/2009ja015143

Hayakawa, M., A. Schekotov, J. Izutsu, S.-S. Yang, M. Solovieva and Y. Hobara (2022). Multi-parameter observations of seismogenic phenomena related to the Tokyo earthquake (M = 5.9) on 7 October 2021, Geosciences, 12, 7, 265, https://doi.org/10.3390/geosciences12070265

Huang, Q., P. Han, K. Hattori and H. Ren (2020). Electromagnetic signals associated with earthquakes: A Review of Observations, Data Processing, and Mechanisms in China, in Seismoelectric Exploration: Theory, Experiments, and Applications Niels Grobbe, André Revil, Zhenya Zhu, Evert Slob (Editors), American Geophysical Union, 415-436., https://doi.org/10.1002/9781119127383.ch26

Joffe, H., T. Rossetto, C. Bradley and C. O'Connor (2017). Stigma in science: The case of earthquake prediction, Disasters, 42, 1, 81-100, https://doi.org/10.1111/disa.12237

Nature Editorial (2023). Syria after the earthquakes: how researchers help. Nature, 615, 7, https://doi.org/10.1038/d41586-023-00571-7

Nomikos, K. and F. Vallianatos (1998). Electromagnetic variations associated with the seismicity of the frontal Hellenic Arc, Geol. Carpath., 49, 57-60.

Nomikos, K., M. Bakatsakis, D. Paterakis, T. Kogionis, E. Sideris, V. Zaxaropoulos, C. Cristou, J. Kaliakatsos and F. Vallianatos (1995). Development of a telemetric system for observation of radio emission associated with earthquakes in Crete island, in Proceedings XXIV General Assembly, European Seismological Commission, Athens, Greece, 1112-1120.

Nomikos, K., F. Vallianatos, I. Kaliakatsos, E. Sideris and M. Bakatsakis (1997). The latest aspects of telluric and electromagnetic variations associated with shallow and intermediate depth earthquakes in the south Aegean, Ann. Geophys., 40, 2. https://doi.org/10.4401/ag-3919

Kalligeris, N., V. Skanavis, M. Charalampakis, N.S. Melis, E. Voukouvalas, A. Annunziato and C.E. Synolakis (2022). Field survey of the 30 October 2020 Samos (Aegean Sea) tsunami in the Greek islands. Bull. Earthquake Eng. 20, 7873-7905, https://doi.org/10.1007/s10518-021-01250-6

Kapiris, P.G., K.A. Eftaxias and T.L. Chelidze (2004a). Electromagnetic signature of prefracture criticality in Heterogeneous Media, Phys. Rev. Let., 92, 6, https://doi.org/10.1103/physrevlett.92.065702

Kapiris, P.G., G.T. Balasis, J.A. Kopanas, G.N. Antonopoulos, A.S. Peratzakis and K.A. Eftaxias (2004b). Scaling similarities of multiple fracturing of solid materials, Non. Proc. Geophys., 11, 1, 137-151, https://doi.org/10.5194/npg-11-137-2004

Karamanos, K., D. Dakopoulos, K. Aloupis, A. Peratzakis, L. Athanasopoulou, S. Nikolopoulos, P. Kapiris, and K. Eftaxias (2006). Study of preseismic electromagnetic signals in terms of complexity, Phys. Rev. E, 74, 1, https://doi.org/10.1103/physreve.74.016104

Kazama, M. and T. Noda (2012). Damage statistics (summary of the 2011 off the Pacific coast of Tohoku earthquake damage), Soils and Found., 52, 5, 780-792, https://doi.org/10.1016/j.sandf.2012.11.003

Ke, C.-Y., G.C. McLaskey and D.S. Kammer (2022). Earthquake breakdown energy scaling despite constant fracture energy, Nat. Commun., 13, 1, https://doi.org/10.1038/s41467-022-28647-4

Kefalas, M., J. Kopanas, G. Antonopoulos, G. Koulouras, D. Cavouras, K. Eftaxias, G. Minadakis and C. Nomicos (2011). The telemetric system of Zante station for measuring the electromagnetic variations, Geophys. Res. Abstracts, 13, EGU2011-4480.

Keller, E.A. and D.E. DeVecchio (2019). Natural hazards: Earth's processes as hazards, disasters, and catastrophes, Taylor & Francis Group, London. https://doi.org/10.4324/9781315164298

Koulouras, G., K. Kontakos, I. Stavrakas, J. Stonham and C. Nomicos (2005a). Embedded Compact Flash™ – A new data storage system designed for a data acquisition system, IEEE Circuits and Devices Mag., 21, 4, 27-34. https://doi.org/10.1109/MCD.2005.1492715

Koulouras, G., K. Kontakos, G. Minadakis, I. Stavrakas, J. Stonham and C. Nomicos (2005b). A data acquisition system using compact flash™ memory, in Proceedings of 2nd WSEAS International Conference on Engineering Education, Athens, Greece, 519-524.

Koulouras, G., G. Minadakis, S.M. Potirakis, D. Agiakatsikas, K. Kontakos, E. Tasoulas and C. Nomicos (2014). A data acquisition system for capturing electromagnetic variations, in Proceedings of the eRA – 9 The SynEnergy Forum, The Conference for International Synergy in Energy, Environment, Tourism and contribution of Information Technology in Science, Economy, Society and Education, Piraeus, Greece.

Kraus, J.D. and R.J. Marhefka (2002). Antennas for all applications, McGraw-Hill, New York.

Kumar, R. and A. Misra (2007). Some basic aspects of electromagnetic radiation emission during plastic deformation and crack propagation in Cu-Zn alloys, Mater. Sci. Eng. A., 454-455, 203-210, https://doi.org/10.1016/j.msea.2006.11.011

Lacidogna, G., A. Carpinteri, A. Manuello, G. Durin, A. Schiavi, G. Niccolini and A. Agosto (2010). Acoustic and electromagnetic emissions as precursor phenomena in failure processes, Strain, 47, 144-152, https://doi.org/10.1111/j.1475-1305.2010.00750.x

Lei, X. and T. Satoh (2007). Indicators of critical point behavior prior to rock failure inferred from pre-failure damage, Tectonophysics, 431, 97-111, https://doi.org/10.1016/j.tecto.2006.04.023

Li, P. and M. Cai (2022). Insights into seismicity from the perspective of the crustal stress field: A comment, Nat. Hazards, 111, 1153-1178, https://doi.org/10.1007/s11069-021-05124-7

Li, A., F. Cai, N. Wu, Q. Li, G. Yan, Y. Sun, G. Dong, D. Luo and X. Wang (2021). Structural controls on widespread methane seeps in the back-arc basin of the Mid-Okinawa trough, Ore Geol. Rev., 129, 103950, https://doi.org/10.1016/j.oregeorev.2020.103950

Li, H., Y. Qiao, R. Shen and M. He (2022). Electromagnetic radiation signal monitoring and multi-fractal analysis during uniaxial compression of water-bearing sandstone, Measurement, 196, 111245, https://doi.org/10.1016/j.measurement.2022.111245

Lin, P., P. Wei, C. Wang, S. Kang and X. Wang (2021). Effect of rock mechanical properties on electromagnetic radiation mechanism of rock fracturing, J. Rock Mech. Geotech. Eng., 13, 798-810, https://doi.org/10.1016/j.jrmge.2021.01.001

Martinelli, G. (2020). Previous, current, and future trends in research into earthquake precursors in Geofluids, Geosciences, 10, 189, https://doi.org/10.3390/geosciences10050189

Martinelli, G., P. Plescia and E. Tempesta (2020). Electromagnetic emissions from quartz subjected to shear stress: Spectral signatures and geophysical implications, Geosciences, 10, 140, https://doi.org/10.3390/geosciences10040140

Mastrogiannis, D., S.I. Andreopoulos, S.M. Potirakis, I. Stavrakas, D. Triantis and E.D. Pasiou (2020). Modelling acoustic and electric signals emitted during structural tests in terms of log-periodic power-law models, Mater. Des. & Proc. Commun., 2, https://doi.org/10.1002/mdp2.134

Minadakis, G., S.M. Potirakis, C. Nomicos and K. Eftaxias (2012a) Linking electromagnetic precursors with earthquake dynamics: an approach based on nonextensive fragment and self-affine asperity models, Physica A, 391, 6, 2232-2244, http://dx.doi.org/10.1016/j.physa.2011.11.049.

Minadakis, G., S.M. Potirakis, J. Stonham, C. Nomicos and K. Eftaxias (2012b). The role of propagating stress waves in geophysical scale: Evidence in terms of nonextensivity, Physica A, 391, 22, 5648-5657. http://dx.doi.org/10.1016/j.physa.2012.04.030

Molchanov, O.A. and M. Hayakawa (2008). Seismo-electromagnetics and related phenomena: History and latest results, Terra Scientific Publication Company, Tokyo.

Naddaf, M. (2023). Turkey-Syria earthquake: What scientists know, Nature, 614, 7948, 398-399, https://doi.org/10.1038/d41586-023-00364-y

Ohnaka, M. and K. Mogi (1982). Frequency characteristics of acoustic emission in rocks under uniaxial compression and its relation to the fracturing process to failure, J. Geophys. Res., 87, B5, 3873, https://doi.org/10.1029/jb087ib05p03873

Papadimitriou, K., M. Kalimeri and K. Eftaxias (2008). Nonextensivity and universality in the earthquake preparation process, Phys. Rev. E, 77, 3, 036101/1-14, http://dx.doi.org/10.1103/PhysRevE.77.036101

Picozza, P., L. Conti and A. Sotgiu (2021). Looking for earthquake precursors from space: A critical review. Front. Earth Sci., 9, https://doi.org/10.3389/feart.2021.676775

Politis, D.Z., S.M. Potirakis, P. Malkotsis, N. Papadopoulos, D. Dimakos, M. Exarchos, E. Liadopoulos, Y.F. Contoyiannis, A. Charitopoulos, K. Kontakos, D. Doukakis, G. Koulouras, N. Melis and K. Eftaxias (2023). New features of the ELSEM-Net electromagnetic monitoring stations network and analysis of recent data associated with strong earthquakes, EGU General Assembly 2023, Vienna, Austria, https://doi.org/10.5194/egusphere-egu23-2126

Potirakis, S.M. and D. Mastrogiannis (2017). Critical features revealed in acoustic and electromagnetic emissions during fracture experiments on LIF, Physica A, 485, 11-22, https://doi.org/10.1016/j.physa.2017.05.025

Potirakis, S.M., G. Minadakis, C. Nomicos and K. Eftaxias (2011). A multidisciplinary analysis for traces of the last state of earthquake generation in preseismic electromagnetic emissions, Nat. Hazards and Earth Syst. Sci., 11, 2859-2879, http://dx.doi.org/10.5194/nhess-11-2859-2011

Potirakis, S.M., G. Minadakis and K. Eftaxias (2012a). Analysis of electromagnetic pre-seismic emissions using Fisher information and Tsallis entropy, Physica A, 391, 1-2, 300-306, http://dx.doi.org/10.1016/j.physa.2011.08.003

Potirakis, S.M., G. Minadakis and K. Eftaxias (2012b). Sudden drop of fractal dimension of electromagnetic emissions recorded prior to significant earthquake, Nat. Hazards, 64, 1, 641-650, http://dx.doi.org/10.1007/s11069-012-0262-x

Potirakis, S.M., G. Minadakis and K. Eftaxias (2012c). Relation between seismicity and pre-earthquake electromagnetic emissions in terms of energy, information and entropy content, Nat. Hazards Earth Syst. Sci., 12, 1179-1183, http://dx.doi.org/10.5194/nhess-12-1179-2012

Potirakis, S.M., A. Karadimitrakis and K. Eftaxias (2013). Natural time analysis of critical phenomena: The case of pre-fracture electromagnetic emissions, Chaos, 23, 2, 023117, https://doi.org/10.1063/1.4807908

Potirakis, S.M., Y. Contoyiannis, K. Eftaxias, G. Koulouras and C. Nomicos (2015). Recent field observations indicating an Earth system in critical condition before the occurrence of a significant earthquake, IEEE Geosci. Remote. Sens. Lett., 12, 3, 631-635, https://doi.org/10.1109/lgrs.2014.2354374

Potirakis, S.M., Y. Contoyiannis, N.S. Melis, J. Kopanas, G. Antonopoulos, G. Balasis, C. Kontoes, C. Nomicos and K. Eftaxias (2016). Recent seismic activity at Cephalonia (Greece): A study through candidate electromagnetic precursors in terms of non-linear dynamics, Non. Proc. Geophys., 23, 4, 223-240, https://doi.org/10.5194/npg-23-223-2016

Potirakis, S.M., Y. Contoyiannis, T. Asano and M. Hayakawa (2018). Intermittency-induced criticality in the lower ionosphere prior to the 2016 Kumamoto earthquakes as embedded in the VLF propagation data observed at multiple stations, Tectonophysics, 722, 422-431, https://doi.org/10.1016/j.tecto.2017.11.020

Potirakis, S.M., Y. Contoyiannis and K. Eftaxias (2019a). Lévy and Gauss Statistics in the preparation of an earthquake, Physica A, 528, 121360, https://doi.org/10.1016/j.physa.2019.121360

Potirakis, S.M., A. Schekotov, Y. Contoyiannis, G. Balasis, G.E. Koulouras, N.S. Melis, A.Z. Boutsi, M. Hayakawa, K. Eftaxias and C. Nomicos (2019b). On possible electromagnetic precursors to significant earthquake (Mw = 6.3) occurred in Lesvos (Greece) on 12 June 2017, Entropy, 21, 241, https://doi.org/10.3390/e21030241

Potirakis, S.M., Y. Contoyiannis, A. Schekotov, K. Eftaxias and M. Hayakawa (2021). Evidence of critical dynamics in various electromagnetic precursors, EPJ ST, 230, 1, 151-177, https://doi.org/10.1140/epjst/e2020-000249-x

Potirakis, S.M., Y. Contoyiannis, K. Eftaxias, N.S. Melis and C. Nomicos (2022). Post-spontaneous-symmetry-breaking power-laws after a very strong earthquake: Indication for the preparation of a new strong earthquake or not?, Physica A, 589, 126607, https://doi.org/10.1016/j.physa.2021.126607

Pritchard, M.E., R.M. Allen, T.W. Becker, M.D. Behn, E.E. Brodsky, R. Bürgmann, C. Ebinger, J.T. Freymueller, M. Gerstenberger, B. Haines, Y. Kaneko, S.D. Jacobsen, N. Lindsey, J.J. McGuire, M. Page, S. Ruiz, M. Tolstoy, L. Wallace, W.R. Walter, W. Wilcock and H. Vincent (2020). New opportunities to study earthquake precursors, Seismol. Res. Lett., 91, 5, 2444-2447, https://doi.org/10.1785/0220200089

Pulinets, S. and K. Boyarchuk (2005). Ionospheric precursors of earthquakes, Springer, Heidelberg, https://doi.org/10.1007/b137616

Pulinets, S. and D. Ouzounov (2018). The possibility of earthquake forecasting: Learning from nature, IOP Publishing.

Pulinets, S., D. Ouzounov, A. Karelin and K. Boyarchuk (2022). Earthquake precursors in the atmosphere and ionosphere: New concepts, Springer, Dordrecht. https://doi.org/10.1007/978-94-024-2172-9

Qian, S., J. Yian, H. Cao, S. Shi, Z. Lu, J. Li and K. Ren (1994). Results of the observations on seismoelectromagnetic waves at two earthquake areas, in China, Electromagnetic Phenomena related to Earthquake Prediction M. Hayakawa and Y. Fujinawa (Editors), Terra Scientific Publication Company, Tokyo, Japan, 205-211.

Rabinovitch, A., V. Frid and D. Bahat (2017). Directionality of electromagnetic radiation from fractures, Int. J. Fract., 204, 239-244, https://doi.org/10.1007/s10704-016-0178-7

Schekotov, A., D. Chebrov, M. Hayakawa and G. Belyaev (2021). Estimation of the epicenter position of Kamchatka earthquakes, Pure Appl. Geophys., 178, 813-821, https://doi.org/10.1007/s00024-021-02679-1

Schuster, H.G. (1995). Deterministic Chaos: An Introduction, VCH, Weinheim.

Sharma, S.K., V.S. Chauhan and M. Sinapius (2020). A review on deformation-induced electromagnetic radiation detection: History and current status of the technique, J. Mater. Sci., 56, 4500-4551, https://doi.org/10.1007/s10853-020-05538-x

Song, X., X. Li, Z. Li, Z. Zhang, F. Cheng, P. Chen and Y. Liu (2018). Study on the characteristics of Coal Rock Electromagnetic Radiation (EMR) and the main influencing factors, J. Appl. Geophy., 148, 216-225, https://doi.org/10.1016/j.jappgeo.2017.11.018

Sorokin, V.M., V.M. Chmyrev and M. Hayakawa (2020). A review on electrodynamic influence of atmospheric processes to the ionosphere, Open J. Earthq. Res., 09, 113-141, https://doi.org/10.4236/ojer.2020.92008

Stavrakas, I., M. Clarke, G. Koulouras, G. Stavrakakis and C. Nomicos (2007). Study of directivity effect on electromagnetic emissions in the HF band as earthquake precursors: Preliminary results on field observations, Tectonophysics, 431, 263-271, https://doi.org/10.1016/j.tecto.2006.05.037

Tassoulas, E., A. Vereses, D. Agiakatsikas, G. Koulouras and C. Nomicos (2010). A telemetric system for electromagnetic measurements based on Internet technologies and cloud computing, in Proceeding European Geosciences Union, Geophysical Research Abstracts, Vienna, Austria, SRef-ID: EGU2010-4939.

Tsiriggakis, V., K. Efthimiatos, G. Koulouras, I. Stavrakas, P. Kapiris, K. Ninos, G. Katsimaglis, K. Voudouris, K. Banitsas, K. Eftaxias, A. Koulopoulos, L. Panagiotopoulos and C. Nomicos (2005). A versatile telemetric system based on mixed Internet and wireless transmission, in Proceedings 2nd WSEAS International Conference on Engineering Education, Athens, Greece, 532-536.

Uyeda, S. (2013). On earthquake prediction in Japan, Proc. Jpn. Acad., Ser. B, Phys. Biol. Sci., 89, 391-400, https://doi.org/10.2183/pjab.89.391

Uyeda, S., T. Nagao and M. Kamogawa (2009a). Short-term earthquake prediction: Current status of seismo-electromagnetics, Tectonophysics, 470, 205-213, https://doi.org/10.1016/j.tecto.2008.07.019

Uyeda, S., M. Kamogawa and T. Nagao (2009b). Earthquakes, electromagnetic signals of, Ency. Complex. Syst. Sci., 2621-2635. https://doi.org/10.1007/978-0-387-30440-3_158

Vallianatos, F. and K. Nomikos (1998). Seismogenic radioemissions as earthquake precursors in Greece, Phys. Chem. Earth, 23, 953-957. https://doi.org/10.1016/s0079-1946(98)00126-8

Vance, E. (2018). Natural Disasters: Early Warnings of Terrible Earthquakes Appear High in the Sky, a New Theory Says, Scientific American, Available online: https://www.scientificamerican.com/article/early-warnings-of-terrible-earthquakes-appear-high-in-the-sky-a-new-theory-says/ (accessed on 14 May 2023)

Varotsos, P.A. (2005). The physics of Seismic Electric Signals, Terra Scientific Publication Company, Tokyo, Japan.

Venegas-Aravena, P., E.G. Cordaro and D. Laroze (2019). A review and upgrade of the lithospheric dynamics in context of the seismo-electromagnetic theory, Nat. Hazards Earth Syst. Sci., 19, 1639-1651, https://doi.org/10.5194/nhess-19-1639-2019

Volakis, J.L. (2007). Antenna Engineering Handbook, McGraw-Hill, New York.

Yoshida, S. and T. Ogawa (2004). Electromagnetic emissions from dry and wet granite associated with acoustic emissions, J. Geophys. Res. Solid Earth, 109, https://doi.org/10.1029/2004jb003092

Yoshiro, T. (1991). Low frequency seismogenic electromagnetic emissions as precursors to earthquakes and volcanic eruptions in Japan, J. Sci. Exp., 5, 121-144, http://id.nii.ac.jp/1438/00008767/

Yuan, Y. (2008). Impact of intensity and loss assessment following the Great Wenchuan Earthquake, Earthq. Eng. Eng. Vib., 7, 247-254, https://doi.org/10.1007/s11803-008-0893-9

Zhang, Y., M. Li, Q. Huang, Z. Shao, J. Liu, X. Zhang, W. Ma and M. Parrot (2023a). Statistical correlation between Demeter satellite electronic perturbations and global earthquakes with M ≥ 4.8, IEEE Trans. Geosci. Remote Sens., 61, 1-18, https://doi.org/10.1109/tgrs.2023.3265931

Zhang, F.-Z., J.-P. Huang, Z. Li, X.-H. Shen, W.-J. Li, Q. Wang, Z. Zeren, J.-L. Liu, Z.-Y. Li and Z.-Y. Chen (2023b). Statistical analysis of electric field perturbations in ELF based on the CSES Observation Data before the earthquake, Front. Earth Sci., 11, 1-13, https://doi.org/10.3389/feart.2023.1101542

Zhao, X., S. Pan, Z. Sun, H. Guo, L. Zhang and K. Feng (2021). Advances of satellite remote sensing technology in earthquake prediction, Nat. Hazards Rev., 22, 03120001, https://doi.org/10.1061/(asce)nh.1527-6996.0000419

Zhao, G., X. Zhang, J. Cai, Y. Zhan, Q. Ma, J. Tang, X. Du, B. Han, L. Wang, X. Chen, Q. Xiao, X. Sun, Z. Dong, J. Wang, J. Zhang, Y. Fan and T. Ye (2022). A review of seismo-electromagnetic research in China, Sci. China Earth Sci, 65, 1229-1246, https://doi.org/10.1007/s11430-021-9930-5

***CORRESPONDING AUTHOR: Stelios M. POTIRAKIS**,
Department of Electrical and Electronics Engineering, Ancient Olive Grove Campus, University of West Attica, Aigaleo-Athens, GR-12241, Greece and Institute for Astronomy, Astrophysics, Space Applications and Remote Sensing, National Observatory of Athens, Metaxa and Vasileos Pavlou, Penteli-Athens, GR-15236, Greece
e-mail: spoti@uniwa.gr